ORIGINAL PAPER

Structural and spectroscopic characterization, electronic properties, and biological activity of the 4-(3-methoxyphenyl)piperazin-1-ium 4-(3-methoxyphenyl)piperazine-1-carboxylate monohydrate

Ceyhun Kucuk[1] · Senay Yurdakul[1] · Namık Özdemir[2] · Belgin Erdem[3]

Abstract

In this study, 4-(3-methoxyphenyl)piperazin-1-ium 4-(3-methoxyphenyl)piperazine-1-carboxylate monohydrate was synthesized and characterized by using spectroscopic (XRD, FT-IR, FT-Ra, and NMR) techniques. Theoretical calculations were performed in the DFT method using the B3LYP functional and the 6–311 + +G(d,p) basis set and compared with the experimental results. It was determined that the geometric parameters and spectroscopic data obtained from the DFT calculations were in high agreement with the experimental results. The HOMO–LUMO energy gap was calculated at 5.19 eV, while this value was experimentally found at 4.26 eV from the UV–Vis absorption spectrum. Although the experimental and theoretical values are different from each other, according to both results, this synthesized structure has low reactivity and a tendency to be stable. Also, the electronic (MEP, Fukuki functions, and charge analyses), nonlinear optical, and thermodynamic properties (heat capacity, entropy, enthalpy change, and Gibbs free energy) of the title complex were investigated. Electrophilic and nucleophilic regions were found to be the same in all of the electronic investigation analyses. The first hyperpolarizability value was calculated to be 25 times (9.27×10^{-30} esu) greater than that of the urea used for comparison. Therefore, it has very good nonlinear optical properties. The change in the values of calculated thermodynamic properties depending on the temperature change shows that the thermodynamic system of the structure changed. Finally, antimicrobial activity studies were carried out to evaluate the biological activity of this synthesized complex, the experimental results were supported by molecular docking studies, and the toxicological and physicochemical properties of the complex were investigated.

Introduction

Piperazines are one of the most important classes of chemical compounds due to their many pharmacological properties. Piperazines consist of a six-membered ring and contain two nitrogen atoms in opposite positions. Most biologically active heterocyclic compounds contain two nitrogen atoms in their structure (Prabavathi et al. 2015). Nitrogen regions in the structures of drug-like molecules increase their solubility in the water and have an important effect on bioavailability (Rathi et al. 2016). Therefore, piperazines are one of the most important chemical compound classes used in new drug discovery, and the piperazine scaffold as a privileged structure is considered to be the core of different therapeutic drug designs (Arbo et al. 2012; Al-Ghorbani et al. 2015). Piperazine and its derivatives exhibit antibacterial, antifungal, anticancer, antiparasitic, antihistamine, psycholytic, and antidepressive activity (Gan et al. 2010). Piperazine citrate is an anthelmintic drug used in the treatment of various worm infections, such as threadworm, roundworm, and pinworm, in humans and animals. This drug prevents the removal of harmful parasites and the spread of diseases by paralyzing the host parasites. Piperazine citrate is also used in the treatment of bacterial infections (Sanad and Mekky 2020).

✉ Senay Yurdakul
  senayy@gazi.edu.tr

[1] Department of Physics, Gazi University, Ankara, Turkey

[2] Department of Mathematics and Science Education, Ondokuz Mayıs University, Samsun, Turkey

[3] Department of Health Care Services, Ahi Evran University, Kırşehir, Turkey

In recent years, bacteria have gained resistance to drugs used in antibacterial and antifungal treatments. Therefore, many problems are waiting to be solved with new drug designs (Tahir et al. 2019). In a previous study, levofloxacin carrying a 2-aryl-2-oxoethyl or a 2-aryl-2-oxyiminoethyl moiety was added to the piperazine ring. Antibacterial evaluation of these synthesized structures was studied and showed better activity against gram-positive bacteria than their main quinolones, levofloxacin and *N*-desmethyl levofloxacin (Foroumadi et al. 2007). In the other study, the *N*-[2-(thiophen-3-yl) ethyl] piperazinyl moiety was added to the 7-position of the quinolone ring to create new quinolone agents. Ciprofloxacin derivatives containing *N*-[2-(thiophen-3-yl)-2-hydroxyimino ethyl] or *N*-[2-(thiophen-3-yl)-2-methoxyiminoethyl] demonstrated greater activity against gram-positive bacteria than the reference drugs norfloxacin and ciprofloxacin (Latefat et al. 2007). According to literature investigations, it has been stated that piperazine derivatives such as 1-(5-chloro-2-methoxybenzoyl)-4-(3-chlorophenyl) piperazine (Weiderhold et al. 2006) and 2-(2-(4-substituted piperazine-1-yl)-5-phenylthiazol-4-yl)-3-aryl quinazolinone (Sharma and Ravani 2013) can be used as anticancer agents and contribute to the inhibition of various cancer cells.

In addition, there are many biological activity studies of piperazine-containing carboxylate syntheses in the literature. In one of these studies, a new ethyl-(E)-4-(2-(2-arylidenehydrazinyl)-2-oxoethyl)piperazine-1-carboxylate series (hydrazones) was designed. It was determined that these synthesized synthetic hydrozones showed antibacterial and antifungal activity against *A. niger*, *K. pneumonia*, *B. subtilis*, *A. flavus*, and *C. neoformans*. Also, experimental spectroscopic and theoretical DFT calculation analyses were performed in this study (Rani et al. 2022). In another study, transition metal complexes of 4-(3,4-dichlorophenyl)piperazine-1-carboxylic acid were synthesized and their crystal structures were analyzed. Moreover, molecular docking and in vitro biological activity studies on the urease inhibitory properties of the synthesized complexes were reported (Chen et al. 2006).

Except for piperazine-containing carboxylate studies, there are also many spectroscopic, electronic, optical, and thermodynamic properties as well as microbiological activity studies for piperazine derivatives. For example, crystal structure investigations, Hirshfeld surface analysis, and DFT studies of 1-[5-(4-methoxy-phenyl)- [1,3,4] oxadiazol-2-yl]-piperazine derivatives were carried out (Kumara et al. 2017). In another study, structural and quantum chemical studies were carried out on aryl sulfonyl piperazine (Abbaz et al. 2019). Many examples of experimental and theoretical research, such as the ones given above, can be found in the literature.

The aim of this study is to determine the spectroscopic, electronic, optical, thermodynamic properties, and antibacterial activity of synthesized 4-(3-methoxyphenyl) piperazin-1-ium 4-(3-methoxyphenyl)piperazine-1-carboxylate monohydrate.

Materials and methods

Computational methods

Quantum chemical calculations were conducted using density functional theory (DFT) with the Becke-3-Lee–Yang–Parr (B3LYP)/6–311 + +G(d,p) basis set approach except for ^{1}H and ^{13}C NMR calculations in the Gaussian09 package version (Dennington et al. 2008; Becke 1993). Also, all visualizations were performed with the Gauss View 5.0 program (Frisch et al. 2009). Firstly, the initial geometry of the complex structure obtained from the XRD data was optimized. Then, the optimized molecular structure was used to carry out vibrational frequencies, ^{1}H and ^{13}C NMR analyses, HOMO–LUMO orbitals, global chemical reactivity parameters, MEP analysis, Fukui functions, charge analyses, nonlinear optic properties, and thermodynamic properties of the title complex. The ^{1}H and ^{13}C NMR chemical shifts calculation of the title molecule was performed in ppm relative to TMS at the 6–311 + + (2d,p) basis set by using the Gauge Independent Atomic Orbital (GIAO) (Subashini and Perandy 2016). Hirshfeld surface maps and two-dimensional fingerprint drawings were created with the Crystal Explorer 17 program (Spackman et al. 2021). The molecular docking of the chemical compound–protein interactions was evaluated using AutoDock Vina software. Three-dimensional crystal structures of used proteins were obtained from the RSCB protein data (PDB ID: 4JUR and 4LI3) (https://www.rcsb.org/). The docked complexes were visualized using PYMOL and Discover Studio software (Delano 2002; Biovia 2021). The Osiris Property Explorer program was used to determine the toxic and physicochemical effects of the complex (RSCB PDB Protein Data Bank, http://www.organic-chemistry.org/prog/peo/).

Experimental analyses

FT-IR and FT-Raman spectra were recorded using a Bruker FT-IR spectrometer with ATR equipment and a Jasco FT-Raman spectrometer with an NRS400 confocal microscope. While the FT-IR spectrum was recorded in the regions of 4000–400 cm^{-1}, the FT-Ra spectrum was recorded in the regions of 4000–100 cm^{-1}. Using the Bruker Ultrashield 300 MHz spectrometer, ^{1}H NMR and ^{13}C NMR spectra of the title complex were recorded in the range of 0–15 and 100–200 ppm, respectively, in DMSO solvent. The UV–Vis spectrum was recorded in the range

of 190–1100 nm in DMSO solvent by using an Agilent HP 8453 spectrophotometer.

Synthesis method

1-(3-Methoxyphenyl)piperazine was supplied by Sigma-Aldrich Chemical Company and was used without additional purification. 1-(3-Methoxyphenyl)piperazine in 10 ml of ethanol (192 mg, 1 mmol) was dissolved and kept at $+4$ C for 3 months. At the end of this period, crystals suitable for single-crystal X-ray diffraction were grown by slow evaporation.

Antimicrobial and antiquorum sensing activity by the agar well diffusion method

The antimicrobial activity of the newly synthesized compound was determined with the agar well diffusion method according to the National Committee for Clinical Laboratory Standards (NCCLS 2000). For this test, *S. aureus* ATCC 25,923, *B. subtilis* ATCC 6633, *E. faecalis* ATCC 29,212, *L. monocytogenes* ATCC 7644, *S. typhimurium* ATCC 14,028, *K. pneumoniae* ATCC 13,883, *S. dysenteriae* ATCC 11835, *E. coli* ATCC 2592 were evaluated against *P. aeruginosa* ATCC 27,853 and *C. albicans* ATCC 10231.Test microorganisms were put into Nutrient Broth (Difco), where they were cultured for 24 to 48 h. The synthesized chemical was produced as a stock solution in 10% DMSO at a concentration of 100 mg/mL. Using the agar well diffusion technique, bacteria and yeast (1×10^6 per mL) were counted for 24–48 h on Mueller Hinton Agar (Oxoid). Seven-millimeter-diameter wells were drilled into the agar medium, and 70 μl (100 mg/ml) of the chemical was introduced after the wells of the culture plates had been punctured with a sterile cork borer (7 mm in diameter). For 48 h, plates were incubated at 30 °C for yeast and 37 °C for bacteria. The antibiogram zone measurement scale was used to determine the diameter of the test compound's zone of inhibition against bacterial and yeast growth. Ampicillin and cycloheximide were utilized as positive controls, and DMSO (10%) was employed as a negative control. Results are the average of three independent experiments where trials were performed three times. Additionally, the substance's antipathogenic potential and its antiquorum sensing activity against *C. violaceum* ATCC 12,472 on LB agar medium were investigated. A culture of *C. violaceum* (1×10^6) cells was switched on LB agar. After that, cork drills were used to create wells in LB agar, and the tested substance (5 mg/mL) was administered to the wells after being dissolved in 10% DMSO (NCCLS 2003). To examine whether pigment formation around the well was inhibited, plates were incubated at 30 °C for 24 h. Positive results included the development of a transparent halo around the disc and the suppression of bacterial growth.

Determination of antimicrobial activity by minimum inhibitory concentration

According to the NCCLS recommendations, minimum inhibitory concentrations (MIC) for substances against test strains of bacteria and yeast were evaluated (McLean et al. 1997). Mueller–Hinton broth was used for MIC testing, solutions of compounds to be tested (1000 μg/mL in 10% DMSO), and the suspension of bacteria (0.5 McFarland). The microdilution broth method was used to determine MIC values spectrophotometrically in 96-well microtiter plates. The synthesized compounds were produced as 1000 μg/mL stock solutions in 10% DMSO for the MIC test. Stock cultures of bacteria and yeast were created at a density of roughly 1×10^6 cfu/mL in accordance with the McFarland 0.5 turbidity standard. Hundred microliters of inoculum was seeded in duplicate in 96-well plates containing 100 μL of the title compound at concentrations of 500, 250, 125, 62.5, 31.2, 15.6, and 7.8 μg/mL, and the cells were allowed to develop overnight at 37 °C with the flow. A 96-well sterile volume of 100 μL of NB medium was added to all wells of the microtiter plates using an automatic dispenser equipment to determine the MIC using the microdilution broth method (BioTek, Micro Fill). A microplate reader (BioTek, Quant) was used to measure the absorbance at 590 nm wavelength on plates that had been incubated for 24 h at 37 °C. Negative controls included 10% DMSO. The positive control contains the microorganisms.

X-ray crystallography

X-ray data of the title complex were collected with a STOE IPDS II diffractometer at room temperature using graphite-monochromated Mo Kα radiation by applying the -scan method. Data collection and cell refinement were carried out using X-AREA (2002), while data reduction was applied using X-RED32 2002. The structure was solved using the charge-flipping algorithm by SUPERFLIP (Palatinus and Chapuis 2007) and refined by means of the full-matrix least-squares calculations on F^2 using SHELXL-2018 (Sheldrick 2015). The H atoms bonded to the O and N atoms were located in a difference Fourier map and refined freely [O–H$=0.82(3)$–$0.84(4)$ Å and N–H$=0.98(3)$–$0.99(3)$ Å]. All H atoms bonded to C atoms were positioned geometrically and refined as a riding model, fixing the bond lengths at 0.93, 0.97, and 0.96 Å for CH, CH$_2$, and CH$_3$ atoms, respectively. The displacement parameters of the H atoms were fixed at $U_{iso}(H) = 1.2U_{eq}$ ($1.5U_{eq}$ for CH$_3$) of their parent atoms. Crystal data, data collection, and structure refinement

details are given in Table 1. Molecular graphics were generated by using OLEX2 (Dolomanov et al. 2009).

Results and discussion

Description of structure

The solid-state structure of 4-(3-methoxyphenyl)piperazin-1-ium 4-(3-methoxyphenyl)piperazine-1-carboxylate monohydrate has been unambiguously proven by single-crystal X-ray diffraction analysis. Crystal data and structure refinement parameters for the title complex are given in Table 1,

Table 1 Crystal data and structure refinement for 4-(3-methoxyphenyl)piperazin-1-ium 4-(3-methoxyphenyl)piperazine-1-carboxylate monohydrate

CCDC depository	2,063,536
Color/shape	Colorless/plate
Chemical formula	$(C_{11}H_{17}N_2O)^+\cdot$ $(C_{12}H_{15}N_2O_3)^-\cdot H_2O$
Formula weight	446.54
Temperature (K)	296(2)
Wavelength (Å)	0.71073 Mo Kα
Crystal system	Triclinic
Space group	$P-1$ (No. 2)
Unit cell parameters	
a, b, c (Å)	6.5931(5), 10.8807(9), 17.4426(14)
α, β, γ (°)	96.018(7), 97.675(6), 106.828(6)
Volume (Å^3)	1173.32(17)
Z	2
$D_{calc.}$ (g/cm^3)	1.264
μ (mm^{-1})	0.090
Absorption correction	Integration
$T_{min.}, T_{max}$	0.9456, 0.9904
F_{000}	480
Crystal size (mm^3)	$0.79 \times 0.58 \times 0.10$
Diffractometer	STOE IPDS II
Measurement method	ω scan
Index ranges	$-8 \leq h \leq 8, -14 \leq k \leq 14, -23 \leq l \leq 23$
θ range for data collection (°)	$2.150 \leq \theta \leq 28.706$
Reflections collected	21,521
Independent/observed reflections	5993/3769
R_{int}	0.0632
Refinement method	Full-matrix least-squares on F^2
Data/restraints/parameters	5993/0/307
Goodness-of-fit on F^2	1.053
Final R indices [$I > 2\sigma(I)$]	$R_1 = 0.0678, wR_2 = 0.1937$
R indices (all data)	$R_1 = 0.1026, wR_2 = 0.2148$
$\Delta\rho_{max}, \Delta\rho_{min}$ (e/Å^3)	$0.43, -0.41$

and a view of the asymmetric unit showing the atom labeling is presented in Fig. 1.

The compound crystallizes in the triclinic space group $P-1$ with $Z = 2$ and is composed of a singly protonated 4-(3-methoxyphenyl)piperazin-1-ium cation, a 4-(3-methoxyphenyl)piperazine-1-carboxylate anion, and a solvent water molecule. In this organic salt, the NH group of 1-(3-methoxyphenyl)piperazine is protonated, while the OH group of 4-(3-methoxyphenyl)piperazine-1-carboxylic acid is deprotonated. The piperazine rings adopt a chair conformation, as is evident from the puckering parameters (Cremer and Pople 1975), $Q = 0.518(2)$ Å, $q_2 = 0.060(2)$ Å, $q_3 = -0.514(2)$ Å, $\theta = 173.7(2)°$, and $\varphi_2 = 190(2)°$ for the atom sequence N1/C2/C3/N2/C4/C5; $Q = 0.561(2)$ Å, $q_2 = 0.065(2)$ Å, $q_3 = -0.557(2)$ Å, $\theta = 173.4(2)°$, and $\varphi_2 = 163(2)°$ for the atom sequence N3/C13/C14/N4/C15/C16. Atoms N1/N2 and N3/N4 are on opposite sides of the C2/C3/C4/C5 and C13/C14/C15/C16 planes and displaced from these by $-0.63919(5)/0.55474(5)$ and $-0.69345(7)/0.59458(6)$ Å, respectively. The least-squares planes defined by the individual carbon atoms of the phenyl moieties enclose an angle of 78.29(15)°. The bond lengths and angles of the compound show no unusual features (Allen et al. 1987).

There are no intramolecular interactions in the molecular structure of 4-(3-methoxyphenyl)piperazin-1-ium 4-(3-methoxyphenyl)piperazine-1-carboxylate monohydrate. Examination of the structure with PLATON reveals that the compound includes no intramolecular interactions (Spek 2009). In the asymmetric unit, the anion, cation, and water molecule are linked via an intermolecular N3–H3B···O2 and O5W–H5WB···O2 hydrogen bonds. Additional O5W–H5WA···O1 and C16–H16A···O5W hydrogen bonds (Table 2) connect the anions and cations through water molecules into a two-dimensional network along to a axis and generate an $R_3^3(9)$ ring motif (Bernstein et al. 1995). The 2-D networks are associated with each other via N3–H3A···O5W hydrogen bonds, forming a three-dimensional supramolecular network structure (Fig. 2).

Optimized molecular structure

The molecular structure of the title complex was optimized by using the B3LYP functional with the $6-311++G(d,p)$ basis set in the DFT method. The optimized structure is given in Fig. 3. Also, geometric parameters (bond lengths and bond angles) obtained from quantum chemical computations are listed in Table 3. The bond lengths of C_2–C_3, C_4–C_5, C_{13}–C_{14}, and C_{15}–C_{16} bonds in the piperazine rings were calculated to be 1.530, 1.526, 1.527, and 1.525 Å and found to be 1.490, 1.493, 1.517 Å, and 1.513 Å in the XRD analysis, respectively. Also, the C–C bond lengths in the phenyl rings were found in the range of 1.389–1.410 Å in
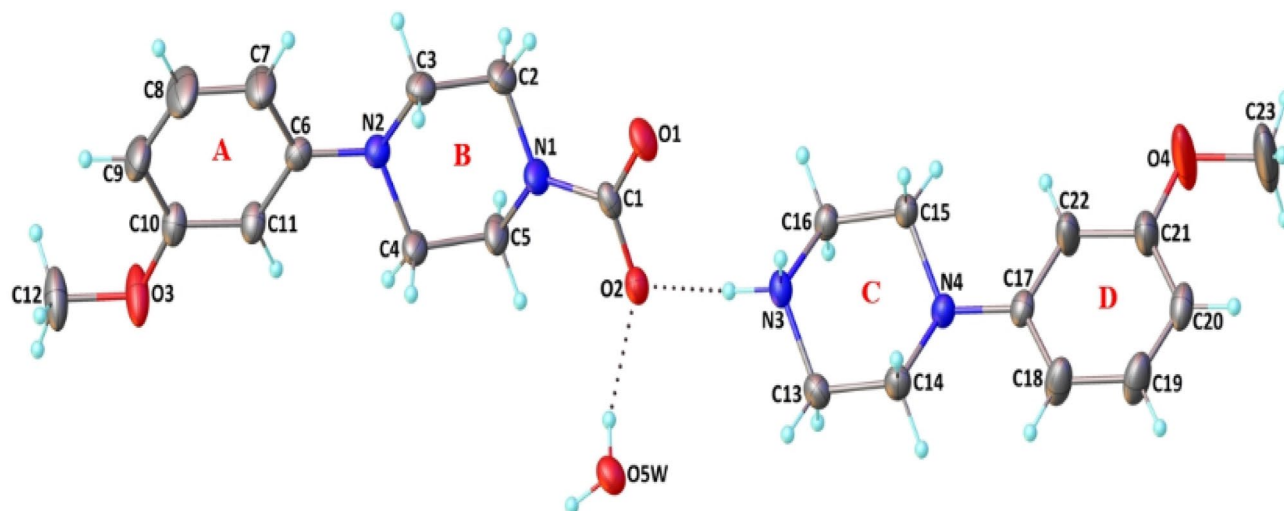
Fig. 1 A view of the asymmetric unit of the title complex showing the atom-labeling scheme. Displacement ellipsoids are drawn at the 20% probability level, and dotted lines display the H-bonding interactions

Table 2 Hydrogen bonding geometry for the title complex

D–H···A	D–H (Å)	H···A (Å)	D···A (Å)	D–H···A (°)
N3–H3B···O2	0.99(3)	1.71(3)	2.697(2)	174(3)
O5W–H5WA···O1[i]	0.84(4)	1.90(4)	2.715(2)	165(3)
N3–H3A···O5W[ii]	0.98(3)	1.86(3)	2.814(3)	165(2)
O5W–H5WB···O2	0.82(3)	1.96(3)	2.752(3)	162(3)
C16–H16A···O5W[iii]	0.97	2.53	3.289(3)	135

the theoretical calculations, while the experimental values were determined in the range of 1.348–1.400 Å. The O_1–C_1 and O_2–C_1 bond lengths were calculated to be 1.329 and 1.234 Å. The XRD values corresponding to these O–C bond length values are 1.249 and 1.279 Å. The computational N–C bond lengths are relatively in harmony with XRD values. The bond lengths for the N_2–C_6 and N_4–C_{17} bonds connecting the imidazole and the phenyl rings were calculated to be 1.413 and 1.410 Å theoretically. Also, these values were found to be 1.400 Å and 1.415 Å from the XRD analysis. While the N–C bond lengths in piperazine rings were calculated in the range of 1.458–1.472 Å, these bond lengths were found in the range of 1.451–1.488 Å, experimentally. The O5W–H5WA and O5W–H5WB bond lengths were found to be 0.981 and 0.961 Å with theoretical calculations. These experimental values were obtained to be 0.840 and 0.820 Å. The calculated bond angle values are very close to the experimental bond angle values. In particular, C–N–C and O–C–O bond angles are in good enough agreement with the XRD data. However, minor deviations in the theoretical and experimental bond angle values of O–C–N emerged. The reason for these small deviations can be explained as follows: In the crystal lattice, the isolated molecule used

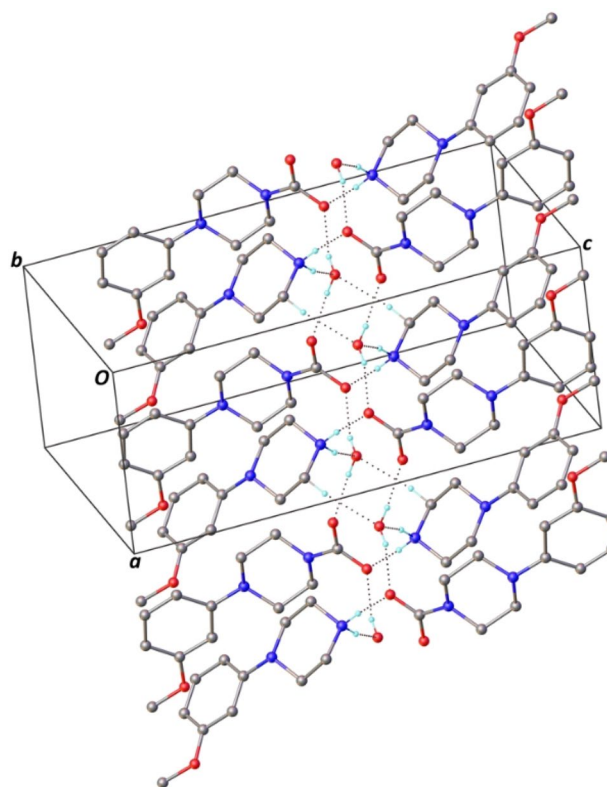**Fig. 2** Part of the crystal structure of the title complex, showing the intermolecular interactions represented by dotted lines

in theoretical experiments interacts Coulombically with neighboring molecules. Furthermore, in addition, quantum chemical calculations were carried out in the gas phase, while XRD data were obtained from the molecule's solid state (Rached et al. 2018; Çelik et al. 2020).

Fig. 3 Optimized molecular structure of title complex
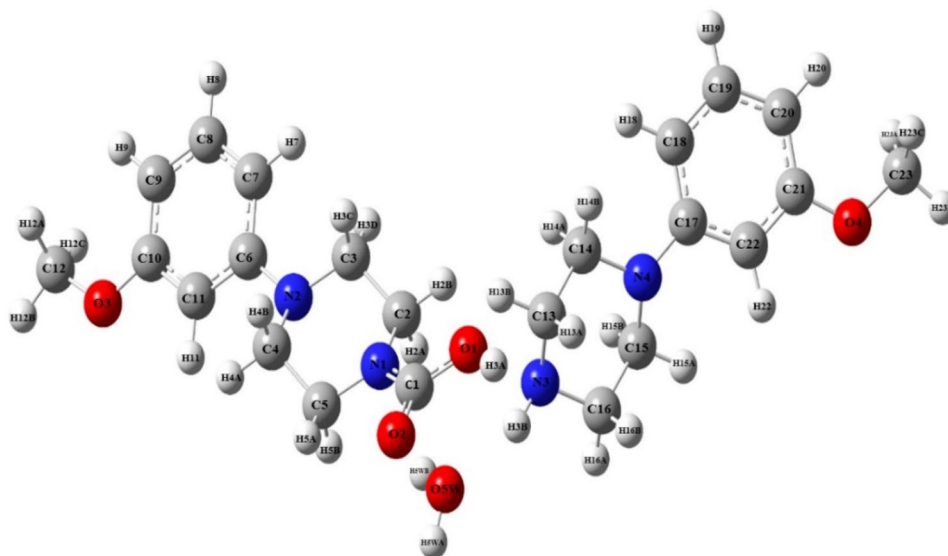
Assignment of vibrational spectra

Some recorded FT-IR and FT-Raman bands and theoretical scaled wavenumbers assigned according to total energy distribution (TED) are given in Table 4, while the other wavenumbers are listed in Supplementary Table S1. Also, experimental FT-IR and FT-Raman spectra are shown in Figs. 4 and 5, respectively. For theoretical wavenumbers, a scale factor of 0.983 was used for values below 1800 cm^{-1} (Govindarajan et al. 2010), while a scale factor of 0.955 was used for values above 1800 cm^{-1} (Çelik et al. 2020).

The O–H stretching vibrations are found in the range of 3400–3800 cm^{-1} (Pieczka et al. 2020). While the symmetrical O–H stretching vibrations were calculated at 3354 and 3249 cm^{-1}, the asymmetrical O–H stretching vibration was calculated at 3722 cm^{-1}. The N–H vibrations for aromatic compounds are observed in the region of 3500–3220 cm^{-1} (Gunasekaran and Anita 2008). This vibration for title compound was calculated at 3249 cm^{-1}. Also, the O–H and N–H stretching vibrations at 2441 cm^{-1} were calculated. In the FT-IR spectrum, these stretching vibrations were observed at 2618 cm^{-1} as a single peak. In a study in the literature, it was stated that carboxylic acid O–H stretching and N–H stretching vibrations indicating the presence of intermolecular hydrogen bonds can be seen in the range of 3000–2400 cm^{-1} (Colmenarez et al. 2017). The H–O–H bending vibrational peaks of water molecules are generally observed between 1700 and 1500 cm^{-1} (Makhloufy et al. 2020). The peaks observed at 1641 and 1637 cm^{-1} in the FT-IR and FT-Ra spectra of the title molecule are the H–O–H bending vibrations of the water molecules in the complex structure. In a study conducted in the literature, the H–O–H bending vibrations of the water molecule of Na-montmorillonite were measured at 1620 cm^{-1} in the FT-IR spectrum (Amarasinghe et al. 2009).

The C–H stretching vibrations for hetero-aromatic compounds are observed in the region of 3100–3000 cm^{-1} (Yurdakul et al. 2015). Some C–H stretching vibrations for the title molecule were calculated at 3068/3070, 3023/3024, 2989/2990, 2951/2952, and 2935 cm^{-1}. These vibration bands were observed at 3087 (vw, IR)/3086 (w/Ra), 3010 (vw, IR)/3019 (w, Ra), 2985 (w, Ra), 2957 (w, IR), and 2935 (vw, IR)/2938 (vw, Ra) cm^{-1}, respectively. In a previous study, the C–H stretching vibrations for 1-(2-methoxyphenyl)piperazine were found at 2993 and 3060 cm^{-1} (FT-IR), and 3000 and 3071 (FT-Ra) (Prabavathi et al. 2015). Also, these values for 1-(2-chlorophenyl)piperazine were observed at 3270 cm^{-1} in the FT-IR spectrum and 3170, 3130, and 3070 cm^{-1} in the FT-Ra spectrum (Prabavathi et al. 2015).

The in-plane C–H bending and the out-of-plane C–H bending vibrations occur in the regions of 1000–1300 and 750–1000 cm^{-1}, respectively (Erdoğdu et al. 2010). The in-plane CCH bending vibrations for the title molecule were calculated at 1222, 1250/1255, 1290, 1339/1344, 1385, 1420, and 1445/1447 cm^{-1}. Experimental values corresponding to the calculated in-plane C–H bending vibrations were observed at 1220 (m/Ra), 1250 (vs/IR), 1282 (s/IR)/1287 (m/Ra), 1340 (m/IR), 1381 (s/IR)/1380 (m/Ra), 1424 (vs/IR)/1415 (s/Ra), and 1445 (m/Ra) cm^{-1}, respectively. Also, one of the calculated out-of-plane CCH stretching vibrations is given at 826 cm^{-1} in Table 4. From the experimental FT-IR and FT-Ra spectra, this value was observed at 828 (s/IR)/ 832 (w/Ra) cm^{-1}. While the in-plane C–H bending vibrations of 1-(2-methoxyphenyl)piperazine were given at 1294, 1270, the out-of-plane C–H bending vibrations were given at 856 and 762 cm^{-1} (Prabavathi et al. 2015).

Table 3 Selected optimized geometrical parameters (bond lengths and bond angles) of the title complex by Becke three Lee–Yang–Parr/6–311 + +G(d,p) in comparison with geometrical parameters of XRD

Parameters	Bond Lengths (Å)		Parameters	Bond angles (°)	
	Calculation	XRD		Calculation	XRD
O_1–C_1	1.329	1.249(2)	C_1–N_1–C_2	124.15	123.17(18)
O_2–C_1	1.234	1.279(3)	C_1–N_1–C_5	120.57	122.79(19)
N_1–C_1	1.365	1.378(3)	C_2–N_1–C_5	114.48	111.79 (18)
N_1–C_2	1.459	1.459(3)	C_3–N_2–C_4	111.62	113.55(17)
N_1–C_5	1.458	1.451(3)	C_3–N_2–C_6	118.14	116.99(17)
N_2–C_3	1.459	1.470(3)	C_4–N_2–C_6	117.26	116.83(17)
N_2–C_4	1.469	1.466(3)	O_1–C_1–O_2	124.29	124.90(2)
N_2–C_6	1.413	1.400(3)	O_1–C_1–N_1	113.53	118.20(2)
N_3–C_{13}	1.472	1.486(3)	O_2–C_1–N_1	122.18	116.88 (17)
N_3–C_{16}	1.472	1.488(3)	N_1–C_2–C_3	110.63	111.02(19)
N_4–C_{14}	1.462	1.466(3)	C_{16}–N_3–C_{13}	110.31	109.29(16)
N_4–C_{15}	1.469	1.470(3)	C_{15}–N_4–C_{14}	112.04	112.94(16)
N_4–C_{17}	1.410	1.415(3)	C_{15}–N_4–C_{17}	117.56	115.96(16)
O_3–C_{10}	1.368	1.363(3)	N_1–C_5–C_4	110.18	111.34(19)
O_3–C_{12}	1.421	1.433(3)	N_2–C_3–C_2	110.72	112.40(2)
O_4–C_{21}	1.368	1.356(4)	N_2–C_4–C_5	111.09	112.75(19)
O_4–C_{23}	1.420	1.444(4)	N_2–C_6–C_7	122.29	122.00(2)
C_2–C_3	1.530	1.490(4)	N_2–C_6–C_{11}	119.51	121.62(18)
C_4–C_5	1.526	1.493(3)	N_3–C_{13}–C_{14}	110.51	110.85(18)
C_6–C_7	1.409	1.400(3)	N_3–C_{16}–C_{15}	110.02	109.91(17)
C_6–C_{11}	1.401	1.371(3)	N_4–C_{14}–C_{13}	110.47	111.88(17)
C_7–C_8	1.390	1.385(5)	N_4–C_{15}–C_{16}	110.89	111.48(17)
C_8–C_9	1.393	1.370(5)	N_4–C_{17}–C_{18}	122.16	122.70(2)
C_9–C_{10}	1.399	1.367(4)	N_4–C_{17}–C_{22}	119.81	120.97(19)
C_{10}–C_{11}	1.394	1.395(3)	O_4–C_{21}–C_{20}	124.17	123.70(3)
C_{13}–C_{14}	1.527	1.517(3)	O_4–C_{21}–C_{22}	115.20	115.20(3)
C_{15}–C_{16}	1.525	1.513(3)	C_6–C_7–C_8	119.99	120.20(3)
C_{17}–C_{18}	1.410	1.388(3)	C_6–C_{11}–C_{10}	121.19	122.00(2)
C_{18}–C_{19}	1.389	1.396(4)	C_7–C_6–C_{11}	118.17	116.30(2)
C_{19}–C_{20}	1.393	1.348(4)	C_7–C_8–C_9	121.91	123.30(3)
C_{20}–C_{21}	1.399	1.373(4)	C_8–C_9–C_{10}	118.17	117.40(3)
C_{21}–C_{22}	1.394	1.395(4)	C_9–C_{10}–C_{11}	120.55	121.10(2)
			C_{10}–O_3–C_{12}	118.55	118.30(2)
			C_{14}–N_4–C_{17}	118.21	116.78(16)
			C_{15}–N_4–C_{14}	112.94	115.96(16)
			C_{15}–N_4–C_{17}	117.55	115.96(16)
			C_{16}–N_3–C_{13}	110.31	109.29.16
			C_{17}–C_{18}–C_{19}	120.08	120.7(3)
			C_{17}–C_{22}–C_{21}	121.25	121.9(3)
			C_{18}–C_{17}–C_{22}	118.00	116.3(2)
			C_{18}–C_{19}–C_{20}	121.95	121.7(3)
			C_{19}–C_{20}–C_{21}	118.08	117.3(2)
			C_{20}–C_{21}–C_{22}	120.62	121.1(3)

Å: Angstrom, °: degree

The C–C stretching vibrations in the aromatic rings generally appear at 1650–1200 cm^{-1} (Ulahannan et al. 2020). These vibrations for title molecule were calculated at 1059, 1102/1103, 1495/1496, 1583, 1619/1620 cm^{-1}.

Experimental C–C stretching vibrations from FT-IR and FT-Ra were observed at 1056 (vw/Ra), 1096 (m/IR), 1494 (s/IR), 1572 (vs/IR), and 1606 (s/IR)/1619 (m/Ra) cm^{-1}. The C–C stretching vibrations were found at 1632, 1596,

Table 4 Detailed assignments of some selected theoretical and experimental frequencies according to the total energy distribution, and normalized absorption intensities of the infrared and Raman spectra of the title complex

Calculated					Observed		
Mode	Fre	Fre[a]	I_{IR}[b]	I_{RA}[b]	IR	Raman	TED
50	583	573	0.55	0.71	575 s	577vw	$12\delta_{CCC} + 13\delta_{CCH}$
51	590	580	0.97	1.23	589 s	–	$10\Gamma_{CNCH}$
52	621	610	0.25	0.29	607w	–	$12\delta_{CCH} + 13\delta_{CCN}$
55	651	640	0.34	0.38	–	644vw	$13\Gamma_{CNCH}$
57/58	699/700	687/688	0.64	0.63	680 s	–	$11\Gamma_{CCCC} + 10\Gamma_{CNCC} + 11\Gamma_{CCCH}$
61	723	711	0.38	0.36	709w	710 m	$10\Gamma_{CNCH} + 11\Gamma_{HNCH}$
62/63	763/765	750/752	0.87	0.76	750 s	756	$11\Gamma_{CCCC} + 33\Gamma_{HNCH}$
66	827	813	0.44	0.34	810 s	–	$13\Gamma_{HCCH} + 10\Gamma_{HNCH}$
67	840	826	0.21	0.16	828 s	832w	$10\gamma_{CCH} + 14\Gamma_{CNCH}$
74	880	865	1.56	1.11	875vw	877vw	$10\Gamma_{HCCH} + 10\Gamma_{CNCH}$
79	971	954	2.31	1.42	951 m	952vw	$13\Gamma_{NCCH}$
83	1007	990	1.61	0.94	990 s	991vs	$13\Gamma_{CNCH}$
84	1012	995	1.21	0.70	998 m	–	$11\Gamma_{CNCH}$
85	1061	1043	1.41	0.76	1040vs	–	$14\delta_{CCH} + 11\Gamma_{CNCC}$
89/90	1077	1059	1.66	0.02	–	1056vw	$10\upsilon_{CC} + 13\upsilon_{CO} + 22\delta_{CCH}$
93/94	1121/1122	1102/1103	0.11	0.07	1096 m	–	$10\upsilon_{CC} + 17\delta_{CCH}$
97	1159	1139	5.98	0.15	1142vs	1143vw	$14\Gamma_{HNCH}$
103/104	1191/1196	1171/1176	4.95	0.07	1174vs	1178vw	$22\delta_{CCH} + 11\Gamma_{CNCH}$
108	1229	1208	6.48	0.12	1214vs	–	$13\delta_{CCH}$
111	1243	1222	5.62	0.04	–	1220 m	$10\upsilon_{CN} + 10\delta_{CCH} + 10\delta_{NCH}$ $+10\Gamma_{CNCH} + 11\Gamma_{NCCH}$
112/113	1272/1277	1250/1255	6.77	0.19	1250vs	–	$10\delta_{CCH} + 10\delta_{NCH} + 10\Gamma_{CNCH}$
116	1312	1290	6.32	0.05	1282 s	1287 m	$17\delta_{CCH} + 11\delta_{NCH} + 13\Gamma_{CNCH}$
122/123	1362/1367	1339/1344	0.53	0.01	1340 m	–	$15\delta_{CCH} + 10\Gamma_{NHCH} + 10\Gamma_{CNCH}$
128	1409	1385	4.66	0.05	1381 s	1380 m	$16\delta_{CCH} + 14\delta_{NCH} + 21\Gamma_{CNCH}$
132	1445	1420	12.76	0.02	1424vs	1415 s	$10\delta_{CCH} + 10\delta_{NCH} + 21\Gamma_{NHCH}$
133/134	1470/1472	1445/1447	0.40	0.04	–	1445 m	$11\delta_{CCH} + 17\delta_{OCH} + 17\delta_{HCH}$
137	1490	1465	0.29	0.06	1466 s	–	$11\delta_{HCH} + 21\Gamma_{CNCH} + 18\Gamma_{HCCH}$
149/150	1521/1522	1495/1496	4.13	0.01	1494 s	–	$11\upsilon_{CC} + 30\delta_{CCH}$
153/154	1610	1583	2.11	0.31	1572vs	–	$22\upsilon_{CC} + 10\delta_{CCC} + 26\delta_{CCH}$
156/157	1647/1648	1619/1620	12.48	0.63	1606 s	1619 m	$35\upsilon_{CC} + 11\delta_{CCC} + 11\delta_{CCH}$
158	1697	1668	11.12	0.14	1641w	1637 s	$10\delta_{HOH}$
159	2556	2441	100.00	1.00	2618w	–	$35\upsilon_{OH} + 27\upsilon_{NH}$
172	3073	2935	0.84	0.16	2935wv	2938vw	$57\upsilon_{CH}$
174/175	3090/3091	2951/2952	0.45	0.10	2957w		$59\upsilon_{CH}$
178/179	3130/3131	2989/2990	0.62	0.20	–	2985w	$80\upsilon_{CH}$
182/183	3165/3167	3023/3024	0.34	0.13	3010vw	3019w	$75\upsilon_{CH}$
188/189	3213/3215	3068/3070	0.07	0.21	3087vw	3086w	$79\upsilon_{CH}$
190	3402	3249	8.53	0.27	3287vw	–	$35\upsilon_{OH} + 29\upsilon_{NH}$
191	3512	3354	28.06	0.20	–	–	$74\upsilon_{OH}$
192	3897	3722	2.23	0.09	–	–	$79\upsilon_{OH}$

υ: stretching, δ: in-plane bending, γ: out-of bending Γ: torsion,

w weak, m medium, s strong, v very

[a]Scaled wavenumbers were calculated by using scaling factors of 0.983 (Govindrajan et al. 2010) and 0.955 (Çelik et al. 2020), respectively, for wavenumbers less and greater than 1800 cm^{-1}

[b] Relative absorption and Raman intensities were normalized with the highest peak absorption equal to 100

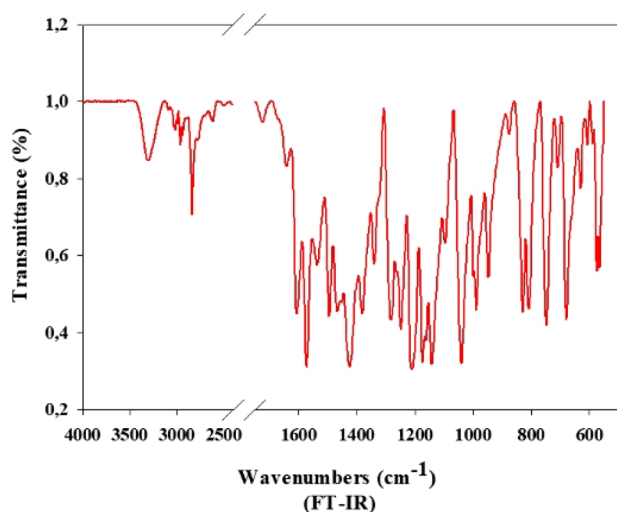[c]Less than 10% of the total energy distribution level (TED) was not given

Fig. 4 Experimental FT-IR spectrum of the title complex
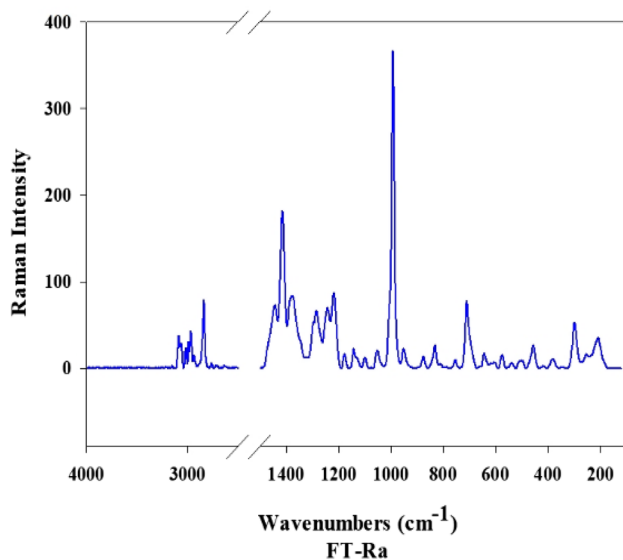

Fig. 5 Experimental FT-Ra spectrum of the title complex

1476, and 1317 cm^{-1} for 1-(2-methoxyphenyl)piperazine and were found at 1631, 1595, 1517, 1453, 1123, 1041, 942, and 869 cm^{-1} for 1-(2-chlorophenyl)piperazine from theoretical calculations. From the FT-IR spectrum, the bands corresponding to these vibrations were observed at 1630, 1591 cm^{-1}, 1318, and 1236 cm^{-1} for 1-(2-methoxy-phenyl)piperazine and at 1590, 1452, 1120, 1040, 942, and 875 cm^{-1} for 1-(2-chlorophenyl)piperazine (Prabavathi et al. 2015).

The C–N vibration was calculated at 1222 cm^{-1}. This vibration was observed at 1220 cm^{-1} (m/Ra). These bands for 3-pyridyl methyl ketone were observed at 1304 and 1194 cm^{-1} in the FT-IR spectrum and were calculated at 1291 and 1221 cm^{-1} (Govindrajan et al. 2010).

The C–O stretching vibration of title compound was calculated at 1059 cm^{-1} and was observed at 1056 cm^{-1} (vw/Ra). While the C–O stretching modes for 3-(bromoacetyl) coumarin were reported at 1216 and 919 cm^{-1}, these modes were obtained at 1297 and 909 cm^{-1} from theoretical calculations (Sarıkaya and Dereli 2013).

In Fig. 6, correlation graphs for infrared and Raman values were created to show the agreement between experimental and theoretical vibration frequencies. According to the R^2 values obtained from the correlation graphs, we can say that the measured and calculated frequency values are quite compatible with each other.

Hirshfeld surface analysis

Hirshfeld surface analysis was performed using the Crystal Explorer 17.5 program to visualize intermolecular interactions in the crystal system (Spackman et al. 2021). The Hirshfeld surface of the crystal structure is formed by the electron distribution, which depends on the sum of the spherical atomic electron densities. The normalized contact distance d_{norm} is given by the following equation as a function of the radii of d_e (the distance from the surface to the nearest nucleus in another molecule), d_i (the distance from the surface to the nearest atom in the molecule itself), and van der Walls (Seth 2014; Arulraj et al. 2020; Cuadradoa et al. 2021).

$$d_{norm} = \frac{d_i - r_i^{VdW}}{r_i^{VdW}} + \frac{d_e - r_e^{VdW}}{r_e^{VdW}} \tag{1}$$

The molecular Hirshfeld surface maps and the associated fingerprint plots are illustrated in Figs. 7 and 8. The red area in the d_{norm} Hirshfeld map shows the more dominant interactions among H atoms, while other visible spots correspond to C–H and O–H contacts. Besides, when the fingerprint drawing plots are examined, it is seen that the interactions contribute to the Hirshfeld surface analysis as a percentage. The H⋯H/H⋯H (60.2%) interactions make up the largest contribution to the Hirshfeld surfaces. These interactions have been represented by the blue spike in the middle. The O⋯H/H⋯O interactions with an 18.4% contribution are given by the blue spikes on the lower left and right, while the C⋯H/H⋯C interactions with an 18.0% contribution are presented in the left and right regions above the O–H.

^{1}H and ^{13}C NMR analyses

The calculated and experimental chemical shift values of the title complex are listed in Table 5 and illustrated in Fig. 9. The experimental ^{1}H and ^{13}C NMR spectra of
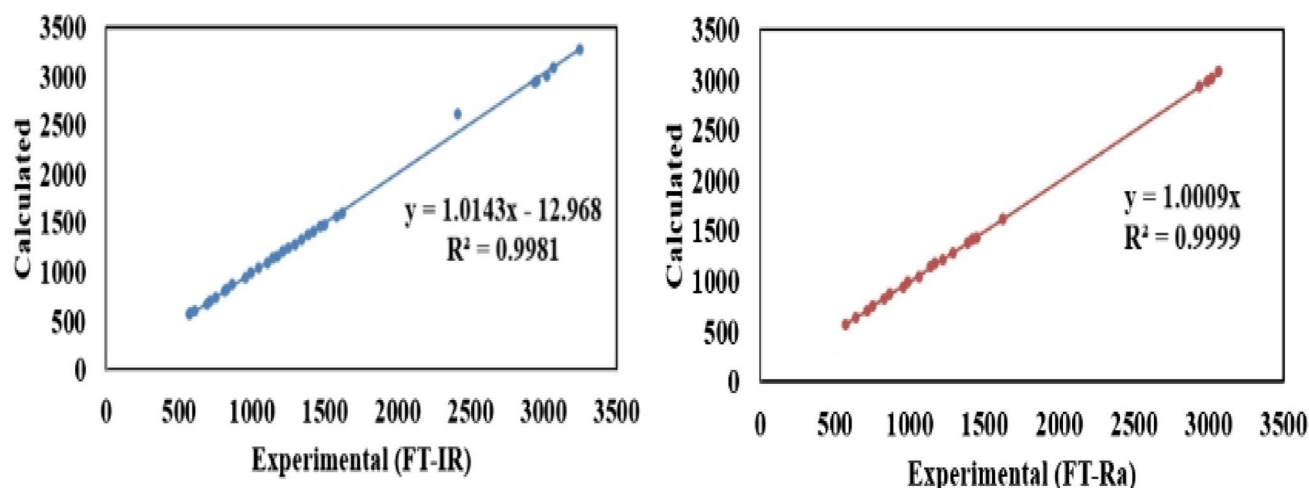
Fig. 6 Correlation graphics between theoretical and experimental wavenumbers (cm^{-1}) of the title complex

the title complex were measured in DMSO solvent. For theoretical calculations, the B3LYP/GIAO model and the 6–311 + G (2d,p) basis set were used (Subashini and Periandy 2016). While experimental ^{1}H NMR and ^{13}C NMR chemical shift values in DMSO solvent were observed in the range of 0.92–9.52 and 39.73–160.65 ppm, respectively, theoretical values were calculated in the range of 0.83–15.16 and 45.51–168.71 ppm. Due to the effect of the O atom, the C$_{12}$ and C$_{23}$ atoms, which are methoxy group carbon atoms, theoretically had low chemical shift values of 55.96 and 55.32 ppm, while experimental values were observed at 65.50 ppm. In the literature, this value for the C atom

Fig. 7 The Hirshfeld surfaces of the title complex mapped over d_{norm} (**a**), d_i (**b**), and d_e (**c**)

of the methoxy group of 1-(2-methoxyphenyl)piperazine was observed at 55.40 ppm and calculated at 60.80 ppm (Prabavathi et al. 2015). The C$_6$ and C$_{17}$ atoms connecting the phenyl ring to the piperazine ring produce a higher chemical shift than the other C atoms, except for the C10 and C21 atoms in the phenyl rings. These chemical shift values were calculated at 160.62 and 160.31 ppm, respectively, and observed at 153.06 ppm. The chemical shift value for the C atom connecting the phenyl ring of the 1-(2-methoxyphenyl)piperazine molecule to the piperazine ring was calculated as 153.90 ppm and observed at 149.7 ppm (Prabavathi et al. 2015). While the chemical shift values for the C$_2$, C$_3$, C$_4$, C$_5$, C$_{13}$, C$_{14}$, C$_{15}$, and C$_{16}$ atoms in the piperazine rings of the title complex were calculated in the range of 45.51–55.49 ppm, they were observed in the range of 39.73–55.30 ppm. Chemical shift values of aromatic carbon atoms give signals between 100 and 150 ppm.

All C atoms except for C$_6$, C$_{10}$, C$_{17}$, and C$_{21}$ in the phenyl rings of the title molecule were measured and calculated in this range. The results obtained for the C atoms in the phenyl ring of the title complex also agree with the results obtained for the phenyl ring of the 1-(2-methoxyphenyl)piperazine molecule (Prabavathi et al. 2015).

From experimental measurements, the methoxy group hydrogen atoms were observed at 3.71 ppm with a sharp singlet peak. This chemical shift value is in good agreement with theoretical values. The H atoms in the piperazine ring of the title complex had chemical shift values in the range of 2.68–4.55 ppm as theoretical, while the experimental values were observed in the range of 2.50–4.60 ppm. Chemical shift values for H atoms in the phenyl ring were calculated and measured in the range of 6.20–8.20 ppm, which is the aromatic proton signal range. The chemical shift values for all the H atoms mentioned above are highly similar to the values of the H atoms in the 1-(2-methoxyphenyl)piperazine
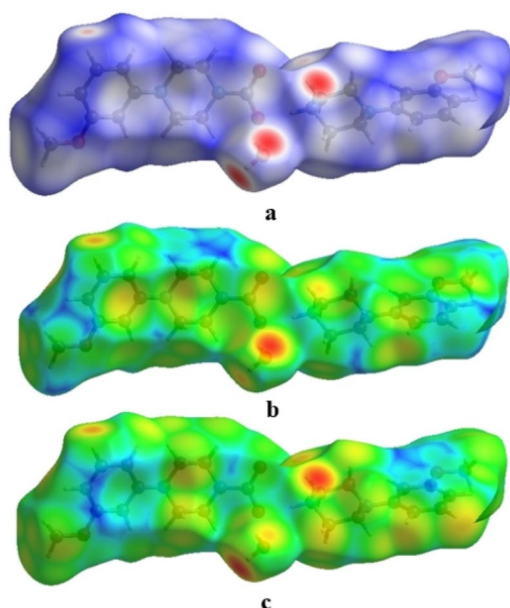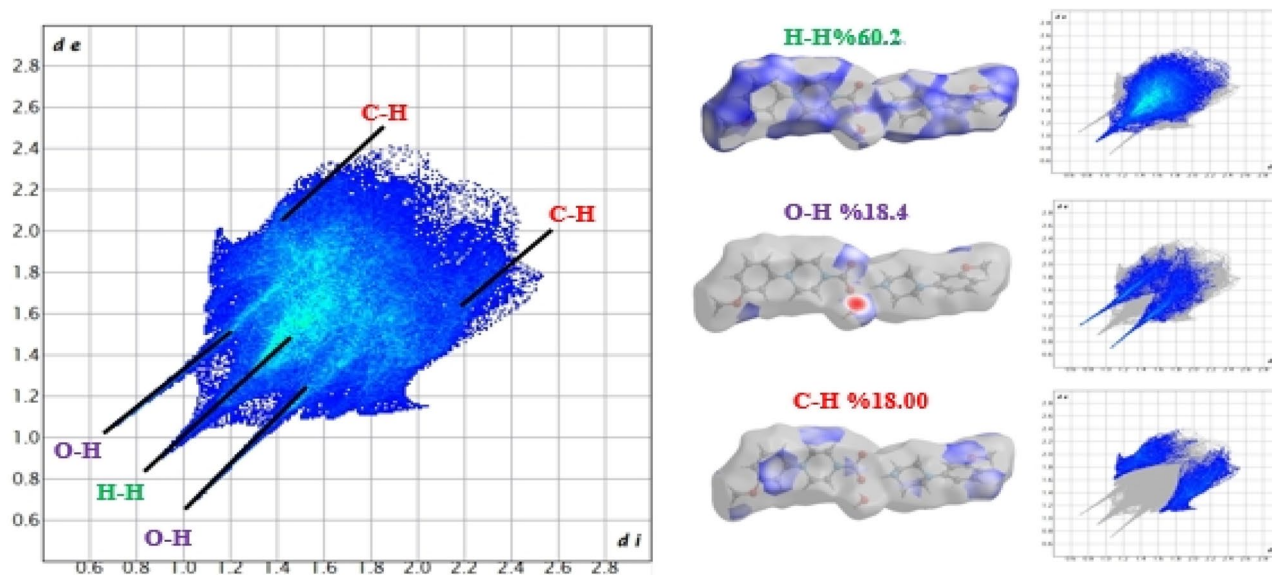
Fig. 8 Two-dimensional fingerprint plots order with a dnorm view of the O–H/H···O (18.4%), H···H (60.2%), C···H/H···C, and (18%) contacts in the title complex

molecule (Prabavathi et al. 2015). In the literature, the chemical shift value of the hydroxyl group H atom of [7-hydroxy3(4-methoxyphenyl)chromone] was observed at 9.72 ppm and calculated at 3.88 ppm (Srivastava et al. 2016). While this value was observed at 9.52 ppm for the H_{3A} atom of the title molecule, it was calculated at 15.16 ppm.

HOMO–LUMO and UV–Vis spectral analyses

Frontier molecular orbitals (FMO) play an important role in finding the electronic and optical properties of a molecule. The highest occupied molecular orbital (HOMO) shows the ability to donate an electron, while the lowest unoccupied molecular orbital (LUMO) shows the ability to receive an electron (Çelik et al. 2020; Erdogdu et al. 2013). These orbitals are also known as boundary molecule orbitals. The HOMO energy is directly related to the ionization potential $(I = -E_{HOMO})$, while the LUMO energy is related to electron affinity $(A = -E_{LUMO})$. Also, global hardness (η), chemical potential (μ^c), electronegativity (χ), and global electrophilicity (ω) values can be calculated from HOMO and LUMO molecular orbital energies using the equations as follows: $\eta = (-E_{HOMO} + E_{LUMO})/2$, $\mu^c = (E_{HOMO} + E_{LUMO})/2$, $\chi = -\mu_c$ and $\omega = \mu^2/2\eta$, respectively (Kumar et al. 2019). The smaller energy difference between these two molecular orbitals, the molecule can be the more polarized. Molecules that can be polarized have very high chemical reactivity and low kinetic stability. Molecules that have this property are soft. As the HOMO–LUMO energy difference increases, the molecule reduces its ability to react. The structures with a high energy gap are called hard molecules (Mishra et al. 2013).

Chemical hardness is the resistance shown to the distribution of electrons in the chemical system, and low chemical hardness indicates that charge transfer occurs within the molecule (Altürk et al. 2015). Chemical potential determines the ability to remove an electron from a molecule in the ground state. The high chemical potential value means that the molecule has an abundance of electron-donating groups (Tamer et al. 2016). The HOMO–LUMO energy values and the other data for the title molecule are given in Table 6.

The HOMO and LUMO energy values of this novelly synthesized complex are −5.59 and −0.40 eV, respectively. The energy gap between these two molecular orbitals of the complex is −5.19 eV. In addition, the energy values of other quantum chemical parameters that determine the reactivity or stability of a molecule were found as follows for the title molecule: I: 5.59 eV, A: 0.40 eV, η: 2.59 eV, χ: 2.99 eV, μc: −2.99 eV, and ω: 1.73 eV. As a result of the calculations made for the synthesized title complex, the HOMO–LUMO energy gap and global hardness values are quite high. Therefore, this molecule has a hard structure with low reactivity, which tends to remain stable. Also, studies in the literature support these results (Oladipo et al. 2021).

The electrostatic contour maps of HOMO and LUMO prepared for 4-(3-methoxyphenyl)piperazin-1-ium 4-(3-methoxyphenyl)piperazine-1-carboxylate monohydrate are given in Fig. 10. While the LUMO is especially distributed over the phenyl (A) ring, the HOMO is distributed over the piperazine (C) and phenyl (D) rings.

The UV–Vis absorption spectrum of this novelly synthesized structure was recorded in the range of 190–1100 nm in DMSO solvent by using an Agilent HP 8453

Table 5 ^{1}H NMR and 13C NMR chemical shift values of the title complex

^{1}H NMR			^{13}C NMR		
Atoms	Calculated	Experimental	Atoms	Calculated	Experimental
H_{2A}	3.01	3.07	C_1	162.87	153.06
H_{2B}	4.23	4.23	C_2	46.27	45.01
H_{3C}	2.68	2.51	C_3	49.87	48.98
H_{3D}	3.17	3.07	C_4	55.15	55.30
H_{4A}	3.68	3.53	C_5	45.73	39.73
H_{4B}	2.71	2.51	C_6	160.62	153.06
H_{5A}	4.23	4.23	C_7	110.41	108.71
H_{5B}	3.02	3.07	C_8	134.68	131.98
H_7	6.51	6.51	C_9	105.23	104.80
H_8	7.60	8.08	C_{10}	167.71	160.65
H_9	6.69	7.13	C_{11}	109.85	102.18
H_{11}	6.76	7.68	C_{12}	55.96	65.50
H_{12A}	3.65	3.71	C_{13}	45.51	39.73
H_{12B}	4.04	3.71	C_{14}	49.43	48.98
H_{12C}	3.70	3.71	C_{15}	53.24	55.30
H_{3A}	15.16	9.52	C_{16}	48.24	48.98
H_{3B}	4.55	4.60	C_{17}	160.31	153.06
H_{13A}	2.88	2.88	C_{18}	110.84	108.71
H_{13B}	3.09	3.07	C_{19}	134.94	131.98
H_{14A}	2.88	2.88	C_{20}	103.17	104.80
H_{14B}	3.24	3.44	C_{21}	168.71	160.65
H_{15A}	3.68	3.53	C_{22}	109.85	102.18
H_{15B}	2.81	2.88	C_{23}	55.32	65.50
H_{16A}	3.03	3.07			
H_{16B}	3.04	3.07			
H_{18}	6.58	6.53			
H_{19}	7.46	8.08			
H_{20}	6.62	7.11			
H_{22}	6.84	7.73			
H_{23A}	3.85	3.71			
H_{23B}	3.94	3.71			
H_{23C}	3.85	3.71			
H_{5WA}	0.83	0.92			
H_{5WB}	5.93	6.17			

spectrophotometer and is presented in Fig. 11. An absorption band was determined at 291 nm, and experimentally determined energy gap value for this absorption band was also found to be 4.26 eV. The energy gap value obtained from the DFT calculations is different from the experimental value. The reason for this is based on the premise in the literature that the band gap energy of the complex comes from the energy-dependent absorption coefficient (α) used in the equation below.

$$\alpha h\upsilon = A(h\upsilon - Eg)^n \tag{2}$$

where α: absorption coefficient, A: constant depends upon material, h: Planck's constant, υ photon frequency, Eg: band gap energy, and n depends upon electron transition (Singh et al. 2022). The energy gap of an organic benzimidazolium benzilate (BDBA) crystal was calculated at 5.251 eV, and this energy value was found to be 4.39 eV from UV–Vis–NIR spectral analysis. It has also been reported that these two values are compatible with each other (Gomathi et al. 2021).

Molecular electrostatic potential (MEP)

MEP is one of the most effective tools used to predict and interpret nucleophilic, electrophilic, and neutral reactive sites. On the map, this process is done according to a color scale (Kumar et al. 2019). While the red color represents the negative electrostatic potential sites, the blue color represents the positive potential sites. The green color also represents the zero potential regions (Ulahannan et al. 2020; Khan et al. 2020). The negativity of the electrostatic potential increases in the following order: red < orange < yellow < green < blue (Çelik et al. 2020; Khan et al. 2020). The electronegative groups are electron-rich regions. The molecular electrostatic potential map of the title molecule is given in Fig. 12. The electrophilic region is especially localized on the O2 atom. Also, O3 and O4 atoms are found in the electron-rich regions. It can be seen from this map that the C atoms in the phenyl rings and the N atoms in the imidazole rings are in the yellow region. Therefore, these C and N atoms are in a slightly electron-rich region. According to this map, almost all of the H atoms in the molecular structure are also in the positive potential region.

Fukui functions

Fukui functions are used to determine important reactive sites on the whole molecule. Fukui functions are also known as indicators of the tendency of the electronic density of the molecule to deform by losing or gaining electrons under the constraint of a fixed external potential (Uzun et al. 2019). Quantum chemical calculations were performed using the B3LYP/6–311 + + G (d, p) basis set to determine the neutral, anionic, and cationic states, and then the Fukui functions were calculated using the following equations (Zacharias et al. 2018).

$$f_k^- = q_k(N) - q_k(N-1) \quad \text{for electrophilic attack} \tag{3}$$

$$f_k^+ = q_k(N+1) - q_k(N) \quad \text{for nucleophilic attack} \tag{4}$$

$$f_k^+ = (1/2)[q_k(N+1) - q_k(N-1)] \quad \text{for neutral (radical) attack} \tag{5}$$
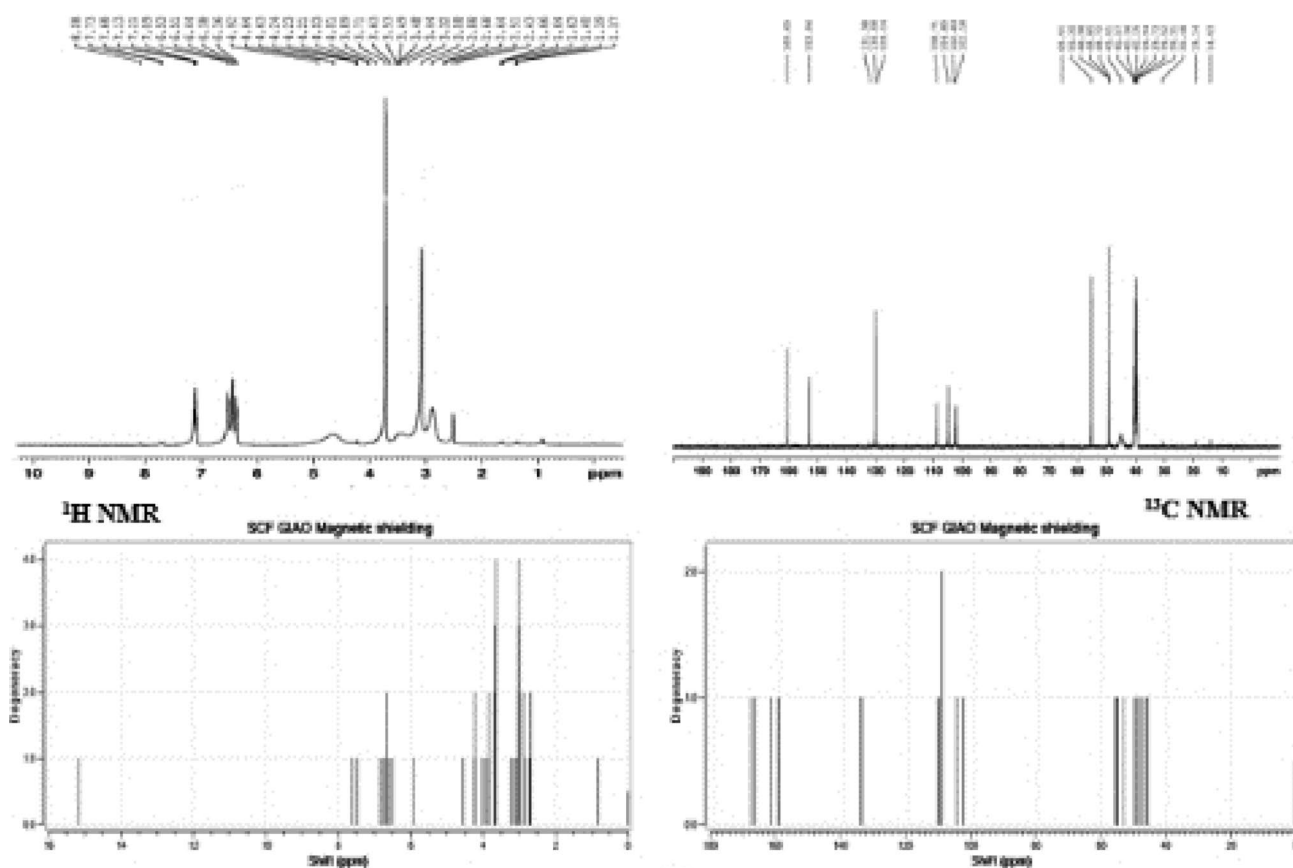
Fig. 9 Experimental and theoretical ^{1}H NMR and ^{13}C NMR spectra of the title complex

In these equations, q_k defines the atomic charge and is the total electron population of k atoms in the N (neutral), $N-1$ (cationic), and $N+1$ (anionic) state (Sethi et al. 2016). When a molecule accepts an electron, the Fukui function is the nucleophilic attack index f_k^+. When a molecule loses an electron, the Fukui function electrophilic attack index is f_k^-. The highest value of the f_k^+/f_k^- ratio is relative electrophilicity, while the highest value of the f_k^-/f_k^+ ratio is relative nucleophilicity (Mumita et al. 2020; Roy et al. 1998). Fukui functions of the title molecule are listed in Table 7.

The maximum value of the electrophilic reactivity descriptors was determined to be the N_4 atom. The second highest electrophilic reactivity descriptor was found at the N2 atom. Also, all C atoms except C_{12}, C_{13}, C_{16}, and C_{23} atoms in the phenyl rings and O_1, O_2, O_3, and O_4 atoms were determined as electrophilic reactivity descriptors. The H_{3A}, H_{3C}, H_{4A}, H_{4B}, H_{5A}, H_7, H_8, H_{11}, H_{14A}, H_{14B}, H_{15A}, and H_{22} atoms are also reactive sites. Also, the other H atoms were determined as the nucleophilic reactivity descriptors from the Fukui functions.

Electrophilic and nucleophilic reactivity regions for the title complex were consistent with each other in MEP map

and Fukui function analyses. As in the Fukui functions, it was also found from the MEP map that O_2, O_3, and O_4 atoms were in the high-reactivity regions, and C and N atoms in the phenyl and imidazole rings were also in the slightly electron-rich region.

Charge analysis

The NBO analysis is one of the important methods used to analyze molecular orbitals and provides information on the reactivity and bonding potential of molecules (Kuruvilla et al. 2018). Also, the atomic charge distribution in the molecular system affects bond types, bond structures, the molecular moment, and many other important properties (Singh et al. 2018; Yurdakul et al. 2019; Büyükmurat and Akyüz 2001). The NBO, Hirshfeld, and APT atomic charge values of the title molecule were calculated using the $6-311++g(d,p)$ basis set and are given in Table 8.

The O and N atoms and C_7, C_9, C_{11}, C_{18}, C_{20}, and C_{22} atoms of the title molecule were found to be electronegative for NBO, APT, and Hirshfeld atomic charge analyses. Furthermore, both NBO and Hirshfeld charges analyses revealed that the C_2, C_3, C_4, C_5, C_{12}, C_{13}, C_{14}, C_{15}, C_{16}, C_{19}, C_{20}, and

Table 6 The energy values of quantum chemical properties of the title complex that calculated at the DFT method using the B3LYP function and 6–311 + +G(d, p) basis set

Molecular orbitals	E (eV)		E_g (eV)	I (eV)	A (eV)	η (eV)	χ(eV)	μ_c(eV)	σ (eV)$^{-1}$	ω(eV)
H	−5.59	ΔE_{H-L}	5.19	5.59	0.40	2.59	2.99	−2.99	0.38	1.73
L	−0.40									
H − 1	−5.68	$\Delta E_{H_{-1}-L_{+1}}$	5.33	5.68	0.35	2.67	3.01	−3.01	0.37	1.70
L + 1	−0.35									
H − 2	−6.16	$\Delta E_{H_{-2}-L_{+2}}$	5.88	6.16	0.28	2.94	3.23	−3.23	0.34	1.77
L + 2	−0.28									

H HOMO, *L* LUMO, E_g energy gap, *I* ionization potential, *A* electron affinity, η global hardness, χ: electronegativity, μ_c chemical potential, σ global softness, ω global electrophilicity, *eV* electron volt, (eV)$^{-1}$: 1/electron volt
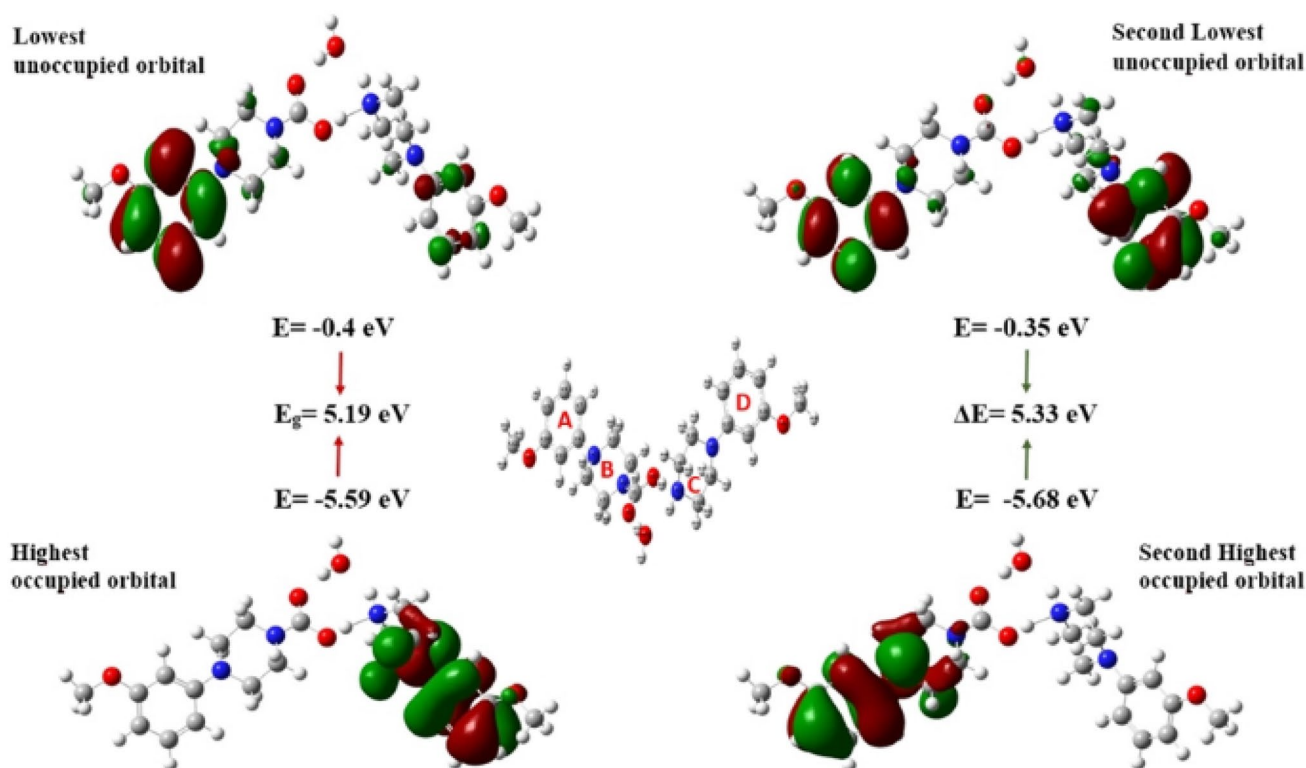

Fig. 10 Frontier molecular orbital diagrams of the title complex to determine the energy gap between molecular orbitals

C_{23} were electronegative. Also, the charge magnitudes of H atoms in the structure were also found positive for the NBO and Hirshfeld analyses. These results obtained from the analysis of the charge are in agreement with the data obtained from both Fukui functions and the molecular electrostatic surface map (MEP).

Nonlinear optical properties

Nonlinear optic materials have an important place in high-technology applications such as frequency shifting, optical modulation, switching, lasers, fiber optic materials, and optical memory. For this reason, the search for materials with nonlinear optical properties has become quite common in recent years (Altürk et al. 2015). The first hyperpolarizability value is associated with the change of π-conjugation length as a result of the interaction of an electron-donating group and an electron-withdrawing group. This conjugation length variation also provides an opportunity to regulate the magnitude of the second-order NLO responses (Lescos et al. 2020). The NLO properties of the title molecule were investigated theoretically by using the B3LYP functional and the 6–311 + +G (d, p) basis set combination in the DFT method. The permanent dipole moment (μ), the
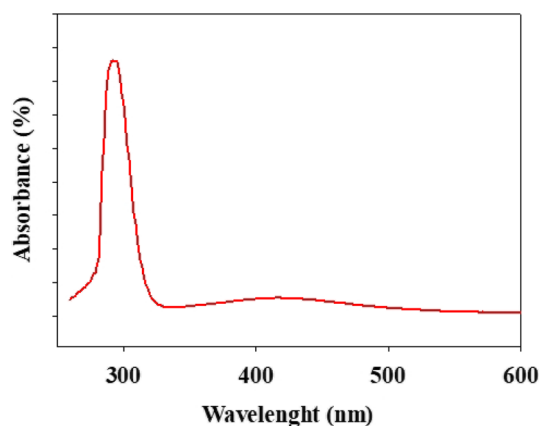
Fig. 11 Experimental UV visible spectrum of the title complex

$$\Delta \alpha = \frac{1}{\sqrt{2}}[(\alpha_{xx} - \alpha_{yy})^2 + (\alpha_{yy} - \alpha_{zz})^2 + (\alpha_{zz} - \alpha_{xx})^2$$
$$+ 6(\alpha_{xy}^2 + \alpha_{yz}^2 + \alpha_{xz}^2)]^{1/2} \quad (8)$$

$$\beta_0 = [(\beta_{xxx} + \beta_{xyy} + \beta_{xzz})^2 + (\beta_{yyy} + \beta_{xxy} + \beta_{yzz})^2$$
$$+ (\beta_{zzz} + \beta_{xxz} + \beta_{yyz})^2]^{1/2} \quad (9)$$

The dipole moment, polarizability, and first hyper-polarizability values are given in Table 9. The dipole moment, average polarizability, anisotropy of polarizability, and the first hyperpolarized value of this new synthesized structure were found to be 2.19D, 51.52×10^{-24}, 24.93×10^{-24}, and 9.27×10^{-30} esu, respectively. The dipole moment (1.3732 D) and first hyperpolarizabil-
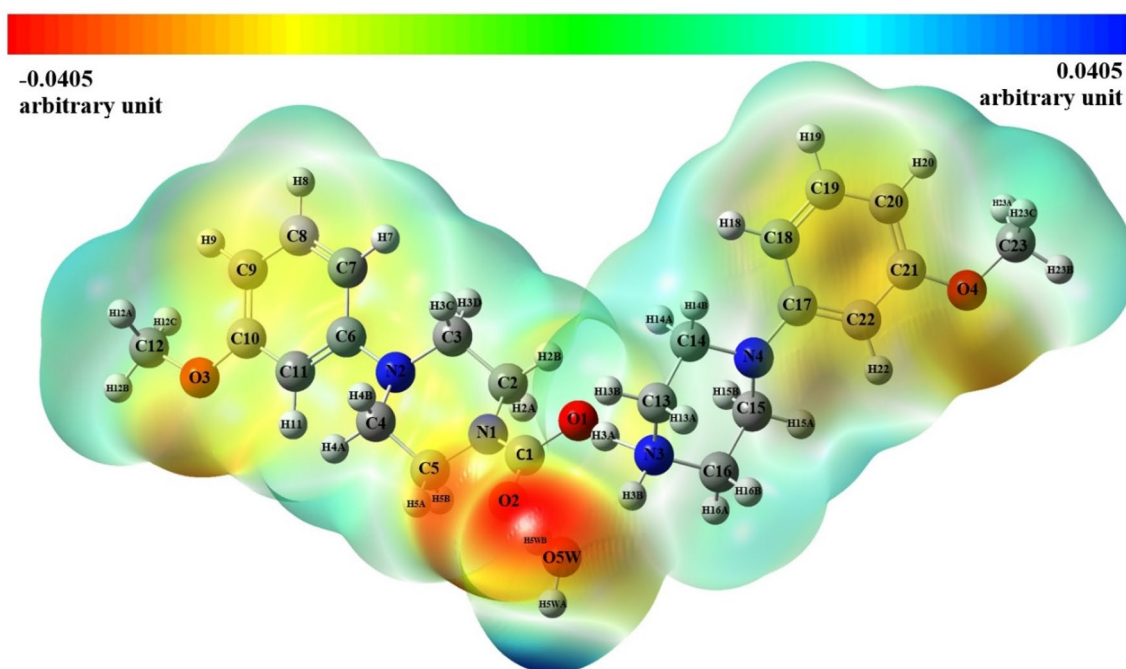

Fig. 12 Molecular electrostatic potential surface map of the title complex in the gas phase

mean polarizability ($\overline{\alpha}$), the anisotropy of the polarizability ($\Delta\alpha$), and the first-order hyperpolarizability (β_0) values were calculated using the equations below (Zhang et al. 2010; Karamanis et al. 2008):

$$\mu^2 = \mu_x^2 + \mu_y^2 + \mu_z^2 \quad (6)$$

$$\overline{\alpha} = (\alpha_{xx} + \alpha_{yy} + \alpha_{zz})/3 \quad (7)$$

ity (0.3728×10^{-30} esu) values of the urea molecule are widely used as standard values for comparison in the literature (Sethi et al. 2016). While the dipole moment value for the synthesized structure was approximately 2 times greater than that of urea, the initial hyperpolarizability value was found to be 25 times greater. According to these results, the title molecule shows very important nonlinear optical properties.

Table 7 The Fukui functions of the title complex are calculated from Hirshfeld charges

Atoms	f^+	f^0	f^-	f^+/f^-	f^-/f^+	Atoms	f^+	f^0	f^-	f^+/f^-	f^-/f^+
O_1	−0.001	0.0005	0.002	−0.50	−2	H_{3A}	0.006	0.006	0.005	1.20	0.83
O_2	0.013	0.001	0.006	2.16	0.46	H_{4A}	0.010	0.001	0.007	1.43	0.70
O_3	0.014	0.0105	0.007	2.00	0.50	H_{5A}	0.010	0.010	0.009	1.11	0.90
O_4	0.015	0.011	0.006	2.50	0.40	H_{12A}	0.008	0.032	0.055	0.15	6.86
O_{5W}	0.001	0.006	0.011	0.09	11.0	H_{13A}	0.011	0.014	0.016	0.69	1.45
N_1	0	0	0	–	–	H_{14A}	0.011	0.001	0.008	1.37	0.72
N_2	0.061	0.032	0.002	30.5	0.03	H_{15A}	0.016	0.012	0.008	2.00	0.50
N_3	0.001	0.001	0.001	1.00	1.00	H_{16A}	0.010	0.011	0.011	0.91	1.10
N_4	0.068	0.035	0.001	68.0	0.01	H_{23A}	0.007	0.028	0.048	0.14	6.86
C_1	0.005	0.005	0.005	1.00	1.00	H_{2B}	0.006	0.007	0.008	0.75	1.33
C_2	0.004	0.005	0.006	0.67	1.50	H_{3B}	0.001	0.002	0.002	0.50	2.00
C_3	0.009	0.008	0.006	1.50	0.67	H_{4B}	−0.259	0.014	0.287	−0.90	−1.11
C_4	0.012	0.008	0.004	3.00	0.33	H_{5B}	0.008	0.009	0.009	0.89	1.13
C_5	0.006	0.006	0.005	1.20	0.83	H_{12B}	0.012	0.037	0.062	0.19	5.17
C_6	0.018	0.012	0.005	3.60	0.28	H_{13B}	0.009	0.011	0.013	0.69	1.44
C_7	0.032	0.021	0.010	3.20	0.31	H_{14B}	0.018	0.012	0.006	3.00	0.33
C_8	0.022	0.020	0.017	1.29	0.77	H_{15B}	0.011	0.012	0.012	0.92	1.09
C_9	0.051	0.033	0.015	3.40	0.29	H_{16B}	0.011	0.012	0.013	0.84	1.18
C_{10}	0.019	0.013	0.006	3.17	0.31	H_{23B}	0.014	0.035	0.055	0.25	3.93
C_{11}	0.022	0.015	0.007	3.14	0.31	H_{3C}	0.018	0.015	0.011	1.64	0.61
C_{12}	0.008	0.028	0.048	0.17	6.00	H_{12C}	0.007	0.029	0.052	0.13	7.43
C_{13}	0.006	0.007	0.008	0.75	1.33	H_{23C}	0.007	0.028	0.048	0.15	6.86
C_{14}	0.012	0.008	0.004	3.00	0.33	H_{3D}	0.010	0.010	0.010	1.00	1.00
C_{15}	0.010	0.008	0.006	1.67	0.60	H_7	0.014	0.013	0.012	1.17	0.85
C_{16}	0.006	0.007	0.007	0.85	1.17	H_8	0.017	−0.059	−0.134	−0.13	−7.88
C_{17}	0.020	0.012	0.004	5.00	0.20	H_9	0.021	0.028	0.034	0.62	1.62
C_{18}	0.035	0.022	0.009	3.89	0.25	H_{11}	0.013	0.011	0.009	1.44	0.69
C_{19}	0.024	0.020	0.016	1.50	0.67	H_{18}	0.015	0.014	0.013	1.15	0.87
C_{20}	0.055	0.035	0.014	3.93	0.25	H_{19}	0.019	0.023	0.026	0.73	1.37
C_{21}	0.019	0.013	0.007	2.71	0.37	H_{20}	0.023	0.026	0.029	0.79	1.26
C_{22}	0.025	0.017	0.008	3.12	0.32	H_{22}	0.015	0.012	0.008	1.86	0.53
C_{23}	0.008	0.027	0.045	0.18	5.63	H_{5WA}	0.008	0.024	0.040	0.20	5.00
H_{2A}	0.008	0.009	0.009	0.89	1.12	H_{5WB}	0.001	0.005	0.008	0.12	8.00

Thermodynamic properties

Thermodynamic parameters of molecules have an effect on the energetic, structural, and reactivity properties of compounds. The values of standard thermodynamic functions such as heat capacity, entropy, enthalpy change, Gibbs free energy, and zero-point energy were calculated on the basis of statistical thermodynamics based on vibrational analysis. The calculated thermodynamic properties in the range of 100–500 K are given in Table 10. Also, changes depending on the temperature are shown in Fig. 13.

The zero point vibration energy of the title complex was found to be 1471.12 kJmol^{-1}. Since this property is characteristic of structure, it is constant at all temperatures. While the entropy, heat capacity, and enthalpy change values of the complex structure increased depending on the rising temperature, the Gibbs free energy value decreased. With the rise in temperature, the vibration between the atoms of the complex increases, causing the entropy and enthalpy changes to increase and the Gibbs free energy to decrease. The change in entropy values shows that the structure changes its thermodynamic system.

Antimicrobial activity studies

The title compound showed highly effective antimicrobial activity against *S. aureus, B. subtilis, E. faecalis, L. monocytogenes, S. typhimurium, K. pneumoniae, S. dysenteriae, E. coli, P. aeruginosa*, and *C. albicans* (Table 11). This synthesized structure revealed potent activity against bacterial and yeast strains, including *E. feacalis, S. typhimurium*, and

Table 8 NBO, Hirschfeld, and APT atomic charge values of the title complex calculated in the DFT method using the B3LYP functional with the 6–311++G(d,p) basis set

| Atoms	APT	NBO	Hirshfeld	Atoms	APT	NBO	Hirshfeld
O_1	−1.231	−0.739	−0.217	H_{3A}	0.313	0.422	0.093
O_2	−1.082	−0.741	−0.302	H_{4A}	−0.002	0.208	0.048
O_3	−0.947	−0.545	−0.145	H_{5A}	0.039	0.237	0.048
O_4	−0.941	−0.546	−0.146	H_{12A}	−0.041	0.168	0.041
O_{5W}	−0.772	−0.977	−0.308	H_{13A}	−0.027	0.201	0.048
N_1	−0.955	−0.526	−0.087	H_{14A}	0.001	0.206	0.046
N_2	−0.889	−0.538	−0.115	H_{15A}	−0079	0.179	0.032
N_3	−0.753	−0.736	−0.129	H_{16A}	−0.071	0.179	0.035
N_4	−0.876	−0.533	−0.113	H_{23A}	−0.041	0.168	0.041
C_1	1.855	0.945	0.238	H_{2B}	0.027	0.232	0.046
C_2	0.327	−0.172	−0.002	H_{3B}	0.804	0.502	0.121
C_3	0.341	−0.179	−0.007	H_{4B}	−0.078	0.176	0.032
C_4	0.341	−0.168	−0.005	H_{5B}	−0.065	0.185	0.038
C_5	0.336	−0.177	−0.002	H_{12B}	0.004	0.190	0.053
C_6	0.706	0.202	0.049	H_{13B}	−0.076	0.178	0.033
C_7	−0.312	−0.283	−0.081	H_{14B}	−0.076	0.179	0.033
C_8	0.174	−0.164	−0.480	H_{15B}	−0.008	0.207	0.046
C_9	−0.312	−0.319	−0.087	H_{16B}	−0.024	0.204	0.050
C_{10}	0.754	0.337	0.071	H_{23B}	−0.005	0.189	0.052
C_{11}	−0.352	−0.276	−0.078	H_{3C}	−0.084	0.175	0.029
C_{12}	0.558	−0.203	−0.010	H_{12C}	−0.039	0.168	0.042
C_{13}	0.328	−0.176	−0.006	H_{23C}	−0.039	0.168	0.042
C_{14}	0.339	−0.172	−0.005	H_{3D}	−0.009	0.208	0.047
C_{15}	0.339	−0.184	−0.007	H_7	0.048	0.207	0.038
C_{16}	0.325	−0.172	−0.004	H_8	0.021	0.201	0.046
C_{17}	0.069	0.204	0.049	H_9	0.049	0.210	0.041
C_{18}	−0.312	−0.284	−0.082	H_{11}	0.062	0.215	0.046
C_{19}	0.175	−0.164	−0.049	H_{18}	0.048	0.207	0.038
C_{20}	−0.316	−0.322	−0.089	H_{19}	0.022	0.201	0.045
C_{21}	0.752	0.337	0.071	H_{20}	0.049	0.209	0.040
C_{22}	−0.351	−0.278	−0.079	H_{22}	0.062	0.214	0.046
C_{23}	0.553	−0.203	−0.010	H_{5WA}	0.257	0.462	0.154
H_{2A}	−0.060	0.185	0.038	H_{5WB}	0.528	0.503	0.109

Table 9 The electric dipole moment μ (Debye), average polarizability $\overline{\alpha}$, anisotropy of polarizability $\Delta\alpha$ $(10^{-24}esu)$, and first hyperpolarizability β_0 $(10^{-30}esu)$ of the title complex

Dipole moment		Polarizability		First Hyperpolarizability			
μ_x	0.51	α_{xx}	65.67	β_{xxx}	2.79	β_x	1.76
μ_y	−2.10	α_{yx}	1.89	β_{xxy}	−4.21	β_y	−7.85
μ_z	−0.35	α_{yy}	50.92	β_{xyy}	−1.68	β_z	4.62
μ	2.19	α_{zx}	2.11	β_{yyy}	−3.88	β_{tot}	9.27
		α_{zy}	−2.65	β_{xxz}	3.06	$\overline{\beta}$	2.76
		α_{zz}	37.97	β_{yxz}	−0.21		
		$\overline{\alpha}$	51.52	β_{yyz}	−0.3		
		$\Delta\alpha$	24.93	β_{zxz}	0.65		
				β_{zyz}	0.24		
				β_{zzz}	1.84		

Table 10 Thermodynamic properties at different temperatures of the title complex at the B3LYP/6–311+ +G(d,p) basis set

T(K)	$C_{p,m}^0$(J mol^{-1} K^{-1})	S_m^0(J mol^{-1} K^{-1})	ΔH_m^0(kJmol^{-1})	ΔG_{corr}(kJmol^{-1})	ε_{zpe}(kJmol^{-1})
100	222.28	526.23	3.38	1435.54	1471.12
200	367.58	731.22	10.64	1369.49	1471.12
300	519.18	911.92	21.41	1287.29	1471.12
400	671.30	1084.75	35.84	1187.47	1471.12
500	805.87	1251.28	53.72	1070.69	1471.12

$C_{p,m}^0$: Heat capacity,S_m^0 Entropy, ΔH_m^0 Enthalpy changes,G_{corr} Gibbs free energy,ε_{ZPE} Zero point energy
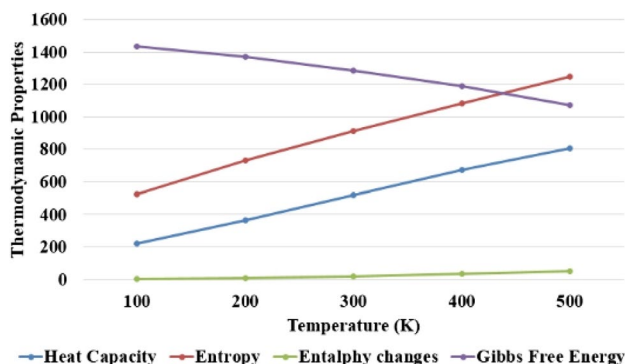
Fig. 13 Thermodynamic properties (heat capacity, entropy enthalpy changes, and Gibbs free energy) of the title complex as a function of temperature in the range of 100–500 K at constant pressure

C. albicans, with a minimum inhibitory concentration (MIC) value of 7.8 µg/mL. Also, this structure against *B. subtilis* and *S. typhimurium* exhibited maximum inhibitory activity with inhibition zone values of 19.8 and 18.4 mm. In comparison with the control ampicillin, compound 5 showed greater antimicrobial activity against *B. subtilis, E. feacalis, E. coli*, and S. typhimurium. The minimum inhibitory concentrations for the same bacteria are 15.6 and 7.8 µg/mL, respectively.

Additionally, the test chemical exhibited antibacterial efficacy against *S. aureus, S. dysenteriae,* and *P. aeruginosa*. The antibacterial activity of this substance was not more potent than that of the antibiotic used as a control, ampicillin.

Antiquorum sensing activity test of the title molecule was performed with *C. violaceum* ATCC 12472, which produces gram-negative and violaceum pigment. The quorum sensing system (QS), which is the communication mechanism between cells in bacteria, controls the pathogenesis and virulence of bacteria. The synthesized title compound created strong anti-QS activity (zone diameter = 20.4 mm and MIC = 7.8 µg/ml).

Molecular docking analysis

Molecular docking is a powerful computational technique used in drug design and discovery. It allows us to understand noncovalent drug–enzyme interactions at the target site of the enzyme (Amul et al. 2019). The AutoDock-Vina program was used to determine the binding ability of the title molecule, its binding mode, and its interactions with

Table 11 Antimicrobial and antiquorum sensing activities of the title complex

Microorganisms	Diameter of inhibition zone (mm) Compound 5		MIC (µg/ml)	AMP (10 µg)	Cyclohex-imide
	(100 mg/ml)	(1000 µg/ml)			
S. aureus ATCC29213	15.8	62.5		17	–
B. subtilis ATCC 6633	19.8	15.6		18	–
E. feacalis ATCC 29212	17.8	7.8		16	–
L. monocytogenes ATCC 7644	14.2	15.6		–	–
S. typhimurium ATCC 14028	18.4	7.8		18	–
K. pneumoniae ATCC 13883	16.2	62.5		–	–
S. dysenteriae ATCC 11835	14.2	31.2		18	–
E. coli ATCC 25922	16.2	15.6		15	–
P. aeruginosa ATCC 27853	17.8	31.2		18	–
*C.albicans*ATCC 10231	16.4	7.8		–	18
C. violeceum ATCC 12472 (QS inhibition (mm))	20.4	7.8		15	–

AMP (10 µg): Ampicillin

Table 12 The binding affinity values of different poses of 4JUR and 4LI3 proteins interaction with the title complex predicted by Autodock Vina

Mode	Affinity (kcal/mol)	Distance from best mode		Affinity (kcal/mol)	Distance from best mode	
		RMSD l.b	RMSD u.b		RMSD l.b	RMSD u.b
	4JUR			4LI3		
1	−7.8	0.000	0.000	−9.8	0.000	0.000
2	−7.8	1.374	2.012	−9.6	1.578	2.188
3	−7.8	1.990	3.032	−9.4	2.336	3.416
4	−7.7	14.538	17.279	−9.3	1.722	10.587
5	−7.6	4.123	6.664	−9.1	2.363	10.637
6	−7.6	14.602	19.827	−9.0	1.388	2.094
7	−7.5	14.516	20.484	−8.8	2.150	3.137
8	−7.5	14.544	19.721	−8.7	5.872	9.633
9	−7.3	1.788	12.696	−8.6	1.969	10.502

the enzyme amino acid residues. In addition, the Auto Dock Tool program (Haruna et al. 2019) was used to prepare the protein and complex in the appropriate format before the molecular docking study. Three-dimensional crystal structures of S. typhimurium ATCC 14028 bacteria used in the antibacterial study section were obtained from the protein data bank (PDB ID: 4JUR and 4LI3) (RSCB PDB Protein Data Bank, https://www.rcsb.org/). The active sites of the protein were defined with a grid size of 40 Å × 40 Å × 40 Å. Minimum binding affinity values of the title molecule to proteins are given in Table 12, and hydrogen bond interactions and acceptor and donor sites are visualized in Fig. 14 and Fig. 15. The minimum binding affinity values of the synthesized complex in the interaction of 4JUR and 4LI3 proteins were determined as −7.8 and −9.8 kcal/mol. A conventional

H bond was formed with the 4JUR protein-bound residues ARG47 and ASN17. The bond lengths in these interactions are 2.57, 2.93, and 2.28 Å, respectively. H-bond interactions with 3.04, 2.18, 2.36, and 2.19 Å bond lengths were formed with SER70, GLY228, and THR 178 residues bound to the 4LI3 protein, respectively. It is a general assumption that a good molecular docking is around 2 based on the RMSD values (Stigliani et al. 2012). These findings also support the antimicrobial activity studies of the synthesized complex and show that this structure has antimicrobial properties.

Toxicological and physicochemical properties

The Osiris Property Explorer Program is one of the tools used to determine whether a compound has a toxic effect on
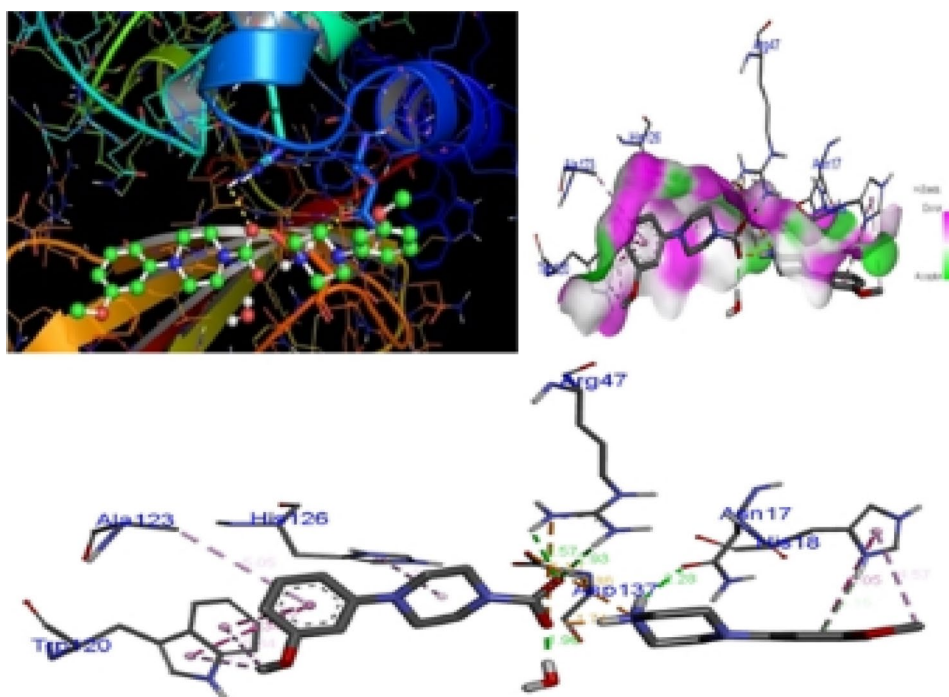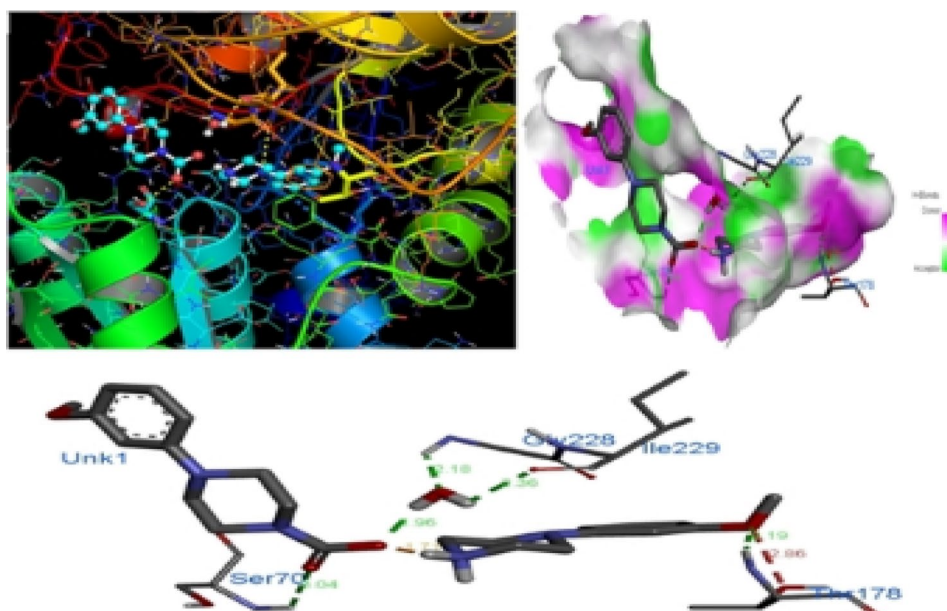

Fig. 14 Molecular docking and hydrogen bond interaction between the title complex and 4JUR protein

Fig. 15 Molecular docking and hydrogen bond interaction between the title complex 4LI3 protein

an organism (http://www.organic-chemistry.org/prog/peo/). The logP value is a measure of the hydrophilicity of the compound. The logP value should not be greater than 5.0 if the compounds are reasonably likely to be absorbed. In some experimental analyses, this value is given as clogP. It is very important to determine the solubility value of LogP in water and lipid since orally consumed drugs pass through the intestinal lining to the aqueous blood stream, reach a cell, and penetrate the lipid-based cell membrane (Uetrecht 2001). The solubility of a compound in water is determined by the logS, which significantly affects the absorption and distribution properties. This value is greater than −4 for more than 80% of the drugs used on the market (http://www.organic-chemistry.org/prog/peo/). The larger the LogS, the higher the absorbability of a compound will be. Due to the low absorption of high-weight compounds, they are prevented them from reaching their target. Therefore, it is necessary to keep the molecular weight as low as possible in drug design. Most commercially available drugs have been reported to have a molecular weight below 450. A molecule must have a TPSA value of less than 140 A^2. The larger this value, the more difficult it is for the structure to pass through the cell membrane (http://www.organic-chemistry.org/prog/peo/; Di and Kerns 2015; Brito 2011). The drug score allows us to evaluate the similarity of a compound to the drug by taking into account clogP, logS, molecular weight, and toxicity risks. If this value is close to 1, it is concluded that a compound can be used as a drug, and if it is close to 0, its use as a drug carries a high risk (http://www.organic-chemistry.org/prog/peo/). The estimated values of the toxicity risk and some important physicochemical properties of the title complex are listed in Table 13. The drug score of the title

molecule was found to be 0.42. Therefore, its use as a drug may pose a high risk. In addition, this structure shows mutagenic, tumorigenic, and reproductive effects.

Conclusion

The synthesized novel organic salt compound, 4-(3-methoxyphenyl)piperazin-1-ium 4-(3-methoxyphenyl)piperazine-1-carboxylate monohydrate, was characterized by using the single-crystal X-ray diffraction method, ^{1}H NMR, ^{13}C NMR, FT-IR, and FT-Ra spectrometry. Also, the contributions of different intermolecular interactions in the crystal packing motif were investigated by using Hirshfeld surface analysis and associated two-dimensional fingerprint drawings. The initial molecular geometry of the complex structure obtained from the X-ray data was optimized using the DFT method at the B3LYP level with the 6–311 + +G(d,p) basis set. Except for ^{1}H and ^{13}C NMR analyses, the same method and basis set were used for other calculations. Chemical shift values were calculated with the 6–311 + +G(2d,p) basis set. The data obtained from the experimental analyses in the structural characterization studies are quite compatible with the values found in the theoretical calculations. The HOMO–LUMO energy gap and global hardness values of the optimized structure were calculated as 5.19 and 2.59 eV, respectively. According to these results, we said that the title complex has low reactivity and a hard structure. Molecular electrostatic surface (MEP), Fukui functions, and charge analyses were performed to determine the reactive regions of the complex. In all three methods, the reactive regions of the

Table 13 Prediction of toxicity risks and physicochemical properties by Osiris of title complex

Toxicity risks				Physicochemical properties					
Mutagenic	Tumorigenic	Irritant	Reproductive effect	clogP	Solubility	MW	TPSA	Druglikeness	Drugscore
+	+	−	+	0.25	−2.78	446.55	100.73	5.93	0.42

structure were found around the same atoms. The dipole moment and first hyperpolarizability values of the title complex were calculated at 2.19D and 9.27×10^{-30} esu. These results show that this synthesized structure has very good nonlinear optical properties. In addition, changes in thermodynamic functions such as heat capacity, entropy, enthalpy change, Gibbs free energy, and zero point energy depending on temperature were investigated. The change in entropy and enthalpy values with the increase in temperature reveals that the structure changes its thermodynamic system. Antimicrobial activity studies of the synthesized salt complex were carried out. The title complex showed potent activity against bacterial and yeast strains. Also, molecular docking studies were performed to investigate the interactions with the protein structures of microorganisms that are used in antimicrobial activity studies. It has been revealed that this structure interacts with the residue parts of the microorganisms in a way that shows antimicrobial properties. Finally, the toxicological and physicochemical properties of the title complex were investigated. This structure showed mutagenic, tumorigenic, and reproductive effects.

Appendix A: Supplementary data

CCDC 2,063,536 contains the supplementary crystallographic data for the compound reported in this article. These data can be obtained free of charge on application to CCDC, 12 Union Road, Cambridge CB2 1EZ, UK [Fax: +44 1223 336 033, e-mail: deposit@ccdc.cam.ac.uk, https://www.ccdc.cam.ac.uk/structures/].

References

Abbaz T, Bendjeddou A, Villemin D (2019) Structural and quantum chemical studies on aryl sulfonyl piperazine derivatives. J Drug Deliv Ther 9(1s):88–97

Al-Ghorbani M, Bushra BA, Zabiulla S, Mamatha SV, Khanum SA (2015) Piperazine and morpholine: synthetic preview and pharmaceutical applications. J Chem Pharm Res 7(5):281. https://doi.org/10.5958/0974-360X.2015.00100.6

Allen FH, Kennard O, Watson DG, Brammer L, Orpen AG, Taylor R (1987) Tables of Bond Lengths determined by X-Ray and Neutron Diffraction. Part 1. Bond Lengths in Organic Compounds. J Chem Soc Perkin Trans 2(12):1−19.

Altürk S, Tamer Ö, Avcı D, Atalay Y (2015) Synthesis, spectroscopic characterization, second and third-order nonlinear optical properties, and DFT calculations of a novel Mn(II) complex. J Organomet Chem 797:110–119. https://doi.org/10.1016/j.jorganchem.2015.08.014

Amarasinghe PM, Katti KS, Katti DR (2009) Nature of organic fluid–montmorillonite interactions: an FTIR spectroscopic study. J Colloid Interface Sci 337:97–105. https://doi.org/10.1016/j.jcis.2009.05.011

Amul B, Muthu S, Raja M, Sevvanthi S (2019) Spectral, DFT and molecular docking investigations on Etodolac. J Mol Struc 1195:747–761

Arbo MD, Bastos ML, Carmo HF (2012) Piperazine compounds as drugs of abuse. Drug Alcohol Depen 122:174–185. https://doi.org/10.1016/j.drugalcdep.2011.10.007

Arulraj R, Sivakumar S, Rajkumar K, Jasinski JP, Kaur M, Thiruvalluvar A (2020) Synthesis, crystal structure, DFT calculations and Hirshfeld surface analysis of 3-Chloro-3-methyl-r(2), c(6)-bis(p-methoxyphenyl) piperidin-4-one. J Chem Crystallogr 50:41–51

Becke AD (1993) Density-functional thermochemistry III. The role of exact exchange. J Chem Phys 98: 5648.

Bernstein J, Davis RE, Shimoni L, Chang NL (1995) Patterns in hydrogen bonding: functionality and graph set analysis in crystals. Angew Chem Int Ed 34(15):1555–1573

Biovia (2021) Visualization. https://www.3ds.com/products-services/biovia/products/molecular-modeling-simulation/biovia-discovery-studio/visualization/. Accessed 01 October 2021.

Brito MAD (2011) Pharmacokinetic study with computational tools in the medicinal chemistry course. Braz J Pharm Sci 47(4):797–805

Büyükmurat Y, Akyüz S (2001) Theoretical and experimental IR spectra and assignments of 3-aminopyridine. J Mol Struct 563:545–550. https://doi.org/10.1016/S0022-2860(00)00801-2

Chen ZJ, Chen YN, Xu CN, Zhao SS, Cao QY, Qian SS, Jie Q, Zhu HL (2006) Synthesis, crystal structures, molecular docking, and *in vitro* biological activities evaluation of transition metal complexes with 4-(3,4-dichlorophenyl) piperazine-1-carboxylic acid. J Mol Struct 1117:293–299. https://doi.org/10.1016/j.molstruc.2016.03.084

Colmenarez JB, Reinaldo A, Quintero M, Seijas L, Almeida R, Rincón L (2017) Crystal structure analysis and topological study of noncovalent interactions in 2,2-Biimidazole: salicylic acid 2:1 cocrystal. J Chem Crystallogr 47:47–58

Cremer D, Pople JA (1975) General definition of ring puckering coordinates. J Am Chem Soc 97(6):1354–1358

Cuadradoa EP, Ferrer K, Osorioc E, Brito I, Cisterna J, Gutiérrez M (2021) Crystal structure, Hirshfeld surface analysis and DFT studies of N-(4-acetylphenyl)quinoline-3-carboxamide. J Mol Struct 1246:131162

Çelik S, Alp M, Yurdakul S (2020) A combined experimental and theoretical study on vibrational spectra of 3-pyridyl methyl ketone. Spectrosc Lett 53(4):234–248. https://doi.org/10.1080/00387010.2020.1734840

DeLano WL (2002) Pymol: an open-source molecular graphics tool. CCP4 Newslett Prot Crystallogr 40:82–92.

Dennington RD, Keith TA, Millam JM (2008) GaussView 5. Gaussian Inc.

Di L, Kerns EH (2015) Blood-brain barrier in drug discovery: optimizing brain exposure of CNS drugs and minimizing brain side effects for peripheral drugs. Wiley, New York

Dolomanov OV, Bourhis LJ, Gildea RJ, Howard JAK, Puschmann H (2009) A complete structure solution, refinement and analysis program. J Appl Crystallogr 42:339–341

Erdogdu Y, Manimaran D, Güllüoglu MT, Amalanathan M, Joeb IH, Yurdakul S (2013) FT-IR, FT-Raman, NMR Spectra and DFT Simulations of 4-(4-Fluoro-phenyl)-1H-imidazole. Opt Spect 114(4):525–536

Erdoğdu Y, Unsalan O, Sajan D, Gulluoglu M (2010) Structural conformations and vibrational spectral study of chloroflavone with density functional theoretical simulations. Spectrochim Acta A 76:130–136

Foroumadi A, Emami S, Mansouri S, Javidnia A, Saeid-Adeli N, Shirazi FH, Shafiee A (2007) Synthesis and antibacterial activity of levofloxacin derivatives with certain bulky residues on piperazine ring. Eur J Med Chem 42(7):985–992

Frisch MJ, Trucks G, Schlegel UH, Scuseria G, Robb M, Cheeseman J, Barone V, Mennucci B, Petersson G et al (2009) Gaussian 09. Revision C.01; Gaussian, Inc.: Wallingford, CT.

Gan LL, Fang B, Zhou CH (2010) Synthesis of azole-containing piperazine derivatives and evaluation of their antibacterial, antifungal and cytotoxic activities. B Kor Chem Soc 31(12):3684–3692. https://doi.org/10.5012/BKCS.2010.31.12.3684

Gomathi MA, Karnan C, Sivanesan T, Rhoda JC, MAnivannan s, Ragavendran V, Vinitha G, Prabakaran AR (2021) An organic benzimidazolium benzilate (BDBA) crystal: Structural description, spectral investigations, DFT calculations, thermal, photoluminescence, linear and nonlinear optical analysis. Chem Phys Lett 776:138705. https://doi.org/10.1016/j.cplett.2021.138705

Govindarajan M, Ganasan K, Periandy S, Karabacak M, Mohan S (2010) Vibrational spectroscopic analysis of 2-chlorotoluene and 2-bromotoluene: a combined experimental and theoretical study. Spectrochim Acta A Mol Biomol Spect 77(5):1005–1013

Gunasekaran S, Anita B (2008) Spectral investigation and normal coordinate analysis of piperazine. Indian J Pure Ap Phy 46:833–838

Haruna K, Kumar VS, Maray YS, Popoola SA, Thomas R, Roxy MS, Al-Saadi AA (2019) Conformational profile, vibrational assignments, NLO properties and molecular docking of biologically active herbicide1,1-dimethyl-3-phenylurea. Heliyon 5:01987

Karamanis P, Pouchan C, Maroulis G (2008) Structure, stability, dipole polarizability and differential polarizability in small gallium arsenide clusters from all-electron ab initio and density-functional-theory calculations. Phys Rev A 77(013201):1–7. https://doi.org/10.1103/PhysRevA.77.013201

Khan B, Khalid M, Shah MR, Tahir MN, Asif HM Aliabad HAR, Hussain A (2020) Synthetic, spectroscopic, SC-XRD and nonlinear optical analysis of potent hydrazide derivatives: A comparative experimental and DFT/ TD-DFT exploration. J Mol Struc 1200:127140. https://doi.org/10.1016/j.molstruct.2019.127140

Kumar S, Radha A, Kour M, Kumar R, Chouaih A, Pandey SK (2019) DFT studies of disubstituted diphenyldithiophosphates of nickel(II): Structural and some spectral parameters. J Mol Struct 1185:212–218

Kumara K, Harish KP, Shivalingegowdac N, Tandond HC, Mohana KN, Lokanath NK (2017) Crystal structure studies, Hirshfeld surface analysis and DFT calculations of novel 1-[5-(4- methoxyphenyl)-[1,3,4]oxadiazol-2-yl]-piperazine derivatives. Chem Data Collect 11(12):40–58

Kuruvilla TK, Prasana JC, Muthu S, George J, Mathew SA (2018) Quantum mechanical and spectroscopic (FT-IR, FT-Raman) study, NBO analysis, HOMO-LUMO, first order hyperpolarizability and molecular docking study of methyl[(3R)-3-(2-methylphenoxy)-3-phenylpropyl]amine by density functional method. Spectrochim Acta A Mol Biomol Spectrosc 188:382–393

Latefat B, Emami S, Mohammadhosseini N, Faramarzi MA, Samadi N, Shafiee A, Foroumadi A (2007) Synthesis and antibacterial activity of New N-[2-(Thiophen-3-yl)ethyl] Piperazinyl Quinolones. Chem Pharm Bull 55(6):894–898

Lescos L, Sitkiewicz SP, Beaujean P, Desce MB, Champagne B, Matito E, Castet F (2020) Performance of DFT functionals for calculating the second-order nonlinear optical properties of dipolar Merocyanines. Phys Chem Phys 22:16579–16594

Makhloufy SE, Majdi EM, Ouasri A, Chtita S, Saadi M, Ammari LE, Cherqaoui A, Belaaouad S (2020) Synthesis, crystal structure, IR, Raman-spectroscopy and DFT computation of monostrontium phosphate monohydrate, $Sr(H_2PO_4)_2 \cdot H_2O$. L Coord Chem 73(16):2328–2346. https://doi.org/10.1080/00958972.2020.1815014

McLean KH, Winson MK, Fish L, Taylor A, Chhabra SR, Camara M, Daykin M, Lamb JH, Swift S, Bycroft BW, Stewart GS, Williams P (1997) Quorum sensing and Chromobacterium violaceum: exploitation of violacein production and inhibition for the detection of N-acyl homoserine lactones. Microbiology 143(12):3703–3711. https://doi.org/10.1099/00221287-143-12-3703

Mishra HN, Kumar SR, Vijay N, Satish C, Kumar SA, Kuamr SV, Onkar P, Leena S (2013) Electronic structure, non-linear properties and Vibrational analysis of ortho, meta and para-Hydroxybenzaldehyde by density functional theory. Res J Rec Sci 2:150–157

Mumita MA, Pala TK, Alam MA, Islama AAM, Paul S, Sheikh MC (2020) DFT studies on vibrational and electronic spectra, HOMO–LUMO, MEP, HOMA, NBO and molecular docking analysis of benzyl-3N-(2,4,5-trimethoxyphenylmethylene) hydrazinecarbodithioate. J Mol Struct 1220:128715

NCCLS (2000) Performance Standards for Antimicrobial Susceptibility Testing: 10th Informational Supplement (Aerobic Dilution, MIC Testing Supplemental Tables. NCCLS document M100-S10(M7), supplement to NCCLS document M7-A5 (MIC testing). National Committee for Clinical Laboratory.

NCCLS (2003) Performance Standards for Antimicrobial Susceptibility Testing:13th Informational Supplement (Disk Diffusion Supplemental Tables). NCCLS document M100-S13 (M2), supplement to NCCLS document M2-A8 (disk diffusion).

Oladipo SD, Tolufashe GF, Mocktar C, Omondi B (2021) Ag(I) symmetrical N, N′ -diarylformamidine dithiocarbamate PPh3 complexes: Synthesis, structural characterization, quantum chemical calculations and in vitro biological studies. Inorg Chim Acta 520:120316

OSIRIS Property Explorer, Allschwil, Switzerland: Actelion Pharmaceuticals Ltd., http://www.organic-chemistry.org/prog/peo/. Accessed October 2021.

Palatinus L, Chapuis G (2007) SUPERFLIP-A computer program for the solution of crystal structures by charge flipping in arbitrary dimensions. J Appl Crystallogr 40:786–790

Pieczka A, Ertl A, Gołębiowska B, Jeleń P, Kotowski J, Nejbert K, Stachowicz M, Giester G (2020) Crystal structure and Raman

spectroscopic studies of OH stretching vibrations in Zn-rich fluor-elbaite. Am Mineral 105:1622–1630

Prabavathi N, Senthil NN, Krishnakumar V (2015) Spectroscopic investigation (FT-IR, FT-Raman, NMR and UV-Vis), conformational stability, NBO and thermodynamic analysis of 1-(2-Methoxyphenyl) Piperazine and 1-(2-Chlorophenyl) Piperazine by DFT approach. Pharm Analy Acta 6(7):2–20. https://doi.org/10.4172/2153-2435.1000391

Rached AB, Maalej W, Guionneau P, Daro N, Mhiri T, Feki H, Elaoud Z (2018) Synthesis, crystal structure, and vibrational and dft simulation studies of benzylammonium dihydrogen phosphate. J Phys Chem Solids 123:150–156

Rani M, Jayanthi S, Kabilan s, Ramachandran R (2022) Synthesis, spectral, crystal structure, hirshfeld surface, computational analysis, and antimicrobial studies of Ethyl-(E)-4-(2-(2-arylidenehydrazinyl)-2-oxoethyl)piperazine-1-carboxylates. J Mol Struct 1252:132082. https://doi.org/10.1016/j.molstruc.2021.132082

Rathi AK, Syed R, Shin HS, Petel RV (2016) Piperazine derivatives for therapeutic use: a patent review (2010-present). Expert Opin the Pat 26(7):777–797. https://doi.org/10.1080/13543776.2016.1189902

Roy RK, Krishnamurti S, Geerlings P, Pal S (1998) Local softness and hardness based reactivity descriptors for predicting ıntra- and ıntermolecular reactivity sequences: carbonyl compounds. J Phys Chem A 102:3746–3755

RSCB PDB Protein Data Bank. https://www.rcsb.org/. Accessed 01 October 2021.

Sanad SMH, Mekky AEM (2020) Synthesis, in-vitro antibacterial and anticancer screening of novel nicotinonitrile-coumarin hybrids utilizing piperazine citrate. Synthetıc Commun 20:1468–1485

Sarıkaya EK, Dereli O (2013) Molecular structure and vibrational spectra of 7-Methoxy-4-methylcoumarin by density functional method. J Mol Struct 1052:214–220. https://doi.org/10.1016/j.molstruc.2013.08.024

Seth SK (2014) Structural elucidation and contribution of intermolecular interactions in *O*-hydroxy acyl aromatics: Insights from X-ray and Hirshfeld surface analysis. J Mol Struct 1064:70–75

Sethi A, Singh RP, Shukla D, Singh P (2016) Synthesis of novel pregnane-diosgenin prodrugs via ring a and ring a connection: a combined experimental and theoretical studies. J Mol Struct 1125:616–623

Sharma RN, Ravani R (2013) Synthesis and screening of 2-(2-(4-substituted piperazine-1-yl)-5-phenylthiazol-4-yl)-3-aryl quinazolinone derivatives as anticancer agents. Med Chem Res 22:2788–2794. https://doi.org/10.1007/s00044-012-0260-2

Sheldrick GM (2015) Crystal structure refinement with SHELXL. Acta Crystallogr C 71:3–8

Singh G, Priyanka DMSS, Devi A, Kaur D, Saini A (2022) Chalcone appended Organosilanes and their silica nanoparticles based UV–vis and fluorometric probes for Co^{2+} ions detection. Inorganica Chim Acta 535:120827. https://doi.org/10.1016/j.ica.2022.120827

Singh P, Islam SS, Ahmad H, Prabaharan A (2018) Spectroscopic investigation (FT-IR, FT-Raman), HOMO-LUMO, NBO, and molecular docking analysis of *N*-ethyl-*N*-nitrosourea, a potential anticancer agent. J Mol Struct 1154:39–50. https://doi.org/10.1016/j.molstruc.2017.10.012

Spackman PR, Turner MJ, McKinnon JJ, Wolff SK, Grimwood DJ, Jayatilaka D, Spackman MA (2021) CrystalExplorer: a program for Hirshfeld surface analysis, visualization and quantitative analysis of molecular crystals. J Appl Cryst 54(3):1006–1011

Spek AL (2009) Structure validation in chemical crystallography. Acta Crystallogr D Biol Crystallogr 65:148–155. https://doi.org/10.1107/S090744490804362X

Srivastava S, Gupta P, Sethi A, Pratap SR (2016) One pot synthesis of Curcumin-NSAIDs prodrug, spectroscopic characterization, conformational analysis, chemical reactivity, intramolecular interactions and first order hyperpolarizability by DFT method. J Mol Struct 1117:173–180. https://doi.org/10.1016/j.molstruc.2016.03.033

Stigliani JL, Genisson VB, Bernadou J, Pratviel G (2012) Cross-docking study on InhA inhibitors: a combination of Autodock Vina and PM6-DH2 simulations to retrieve bio-active conformations. Org Biomol Chem 10:6341–6349

Subashini K, Periandy S (2016) Spectroscopic (FT-IR, FT-Raman, UV, NMR, NBO) investigation and molecular docking study of (R)-2-Amino-1-PhenylEthanol. J Mol Struct 1117:240–256. https://doi.org/10.1016/j.molstruc.2016.03.063

Tahir S, Mahmood T, Dastgir F, Haq I, Waseem A, Rashid U (2019) Design, synthesis and anti-bacterial studies of piperazine derivatives against drug resistant bacteria Eur J Med Chem 166:224–231.

Tamer O, Atalay AS, Avcı D, Atalay Y, Tarcan E, Marchewka MK (2016) Optimized geometry, vibration (IR and Raman) spectra and nonlinear optical activity of p-nitroanilinium perchlorate molecule: a theoretical study. Mater Sci Pol 34(1):192–203

Uetrecht J (2001) Prediction of a new drug's potential to cause idiosyncratic reactions (2001) Curr Opin Drug Discov Dev 4(1):55–59.

Ulahannan RT, Kannan V, Vidya V, Sreekumar K (2020) Synthesis and DFT studies of the structure—NLO activity evaluation of 2-(4-methoxyphenyl)-1,4,5-triphenyl-2,5-dihydro-1H-imidazole. J Mol Struc 1199(127004):1–7. https://doi.org/10.1016/j.molstruc.2019.127004

Uzun S, Esen Z, Koç E, Usta NC, Ceylan M (2019) Experimental and density functional theory (MEP, FMO, NLO, Fukui functions) and antibacterial activity studies on 2-amino-4-(4-nitrophenyl)-5,6-dihydrobenzo [h] quinoline-3-carbonitrile. J Mol Struct 1178:450–457

Weiderhold KN, Randall-Hlubek DA, Polin LA, Hamel E, Mooberry SL (2006) CB694, a novel antimitotic with antitumor activities. Int J Cancer 118:1032–1040. https://doi.org/10.1002/ijc.21424

X-AREA Version, 1.18 and X-RED32 Version 1.04 (2002) Stoe & Cie. Darmstadt, Germany

Yurdakul S, Badoglu S, Gulesci Y (2015) Experimental and theoretical study on Free 5-Nitroquinoline, 5-Nitroisoquinoline, and Their Zinc (II) Halide Complexes. Spectrochim Acta A Mol Biomol Spectr 137:945–956. https://doi.org/10.1016/j.saa.2014.0897

Yurdakul S, Temel E, Buyukgungor O (2019) Crystal structure, spectroscopic characterization, thermal properties and theoretical ınvestigations on [Ag(methyl 4-pyridylketone)2NO3]. J Mol Struct 1191:301–313. https://doi.org/10.1016/j.molstruc.2019.04.071

Zacharias AO, Varghese A, Akshaya KB, Savitha MS, George L (2018) DFT, spectroscopic studies, NBO, NLO and Fukui functional analysis of 1-(1-(2,4-difluorophenyl)-2-(1H-1,2,4-triazol-1-yl) ethylidene) thiosemicarbazide J Mol Struct 1158:1–3.

Zhang R, Du B, Sun G, Sun Y (2010) Experimental and Theoretical Studies on o-, m- and p-Chlorobenzylideneaminoantipyrines. Spectrochim Acta A: Mol Biomol Spectr 75A: 1115–1124. https://doi.org/10.1016/j.saa.2009.12.067